ARMY RESEARCH LABORATORY

ARL

Numerical Prediction of Pitch Damping Stability Derivatives for Finned Projectiles

by Vishal A. Bhagwandin and Jubaraj Sahu

ARL-TR-6725   **November 2013**

NOTICES

Disclaimers

The findings in this report are not to be construed as an official Department of the Army position unless so designated by other authorized documents.

Citation of manufacturer's or trade names does not constitute an official endorsement or approval of the use thereof.

Destroy this report when it is no longer needed. Do not return it to the originator.

Army Research Laboratory

Aberdeen Proving Ground, MD 21005-5066

Numerical Prediction of Pitch Damping Stability Derivatives for Finned Projectiles

Vishal A. Bhagwandin and Jubaraj Sahu
Weapons and Materials Research Directorate, ARL

REPORT DOCUMENTATION PAGE		*Form Approved* *OMB No. 0704-0188*

Public reporting burden for this collection of information is estimated to average 1 hour per response, including the time for reviewing instructions, searching existing data sources, gathering and maintaining the data needed, and completing and reviewing the collection information. Send comments regarding this burden estimate or any other aspect of this collection of information, including suggestions for reducing the burden, to Department of Defense, Washington Headquarters Services, Directorate for Information Operations and Reports (0704-0188), 1215 Jefferson Davis Highway, Suite 1204, Arlington, VA 22202-4302. Respondents should be aware that notwithstanding any other provision of law, no person shall be subject to any penalty for failing to comply with a collection of information if it does not display a currently valid OMB control number.
PLEASE DO NOT RETURN YOUR FORM TO THE ABOVE ADDRESS.

1. REPORT DATE *(DD-MM-YYYY)*	2. REPORT TYPE	3. DATES COVERED (From - To)
xxx 2013	Final	January 2011–June 2012

4. TITLE AND SUBTITLE	5a. CONTRACT NUMBER
Numerical Prediction of Pitch Damping Stability Derivatives for Finned Projectiles	
	5b. GRANT NUMBER
	5c. PROGRAM ELEMENT NUMBER
6. AUTHOR(S)	**5d. PROJECT NUMBER**
Vishal A. Bhagwandin and Jubaraj Sahu	AH80
	5e. TASK NUMBER
	5f. WORK UNIT NUMBER

7. PERFORMING ORGANIZATION NAME(S) AND ADDRESS(ES)	8. PERFORMING ORGANIZATION REPORT NUMBER
U.S. Army Research Laboratory ATTN: RDRL-WML-E Aberdeen Proving Ground, MD 21005-5066	ARL-TR-

9. SPONSORING/MONITORING AGENCY NAME(S) AND ADDRESS(ES)	10. SPONSOR/MONITOR'S ACRONYM(S)
	11. SPONSOR/MONITOR'S REPORT NUMBER(S)

12. DISTRIBUTION/AVAILABILITY STATEMENT

Approved for public release; distribution is unlimited.

13. SUPPLEMENTARY NOTES

14. ABSTRACT

Reynolds-Averaged Navier Stokes computational fluid dynamics and linear flight mechanics theory were used to compute the pitch damping dynamic stability derivatives for two basic finned projectiles using two numerical methods, namely, the transient planar pitching method and the steady lunar coning method. Numerical results were compared to free-flight and wind-tunnel experimental data for Mach numbers in the range 0.5–4.5. The accuracy, efficiency and dependence of these methods on various aerodynamic and numerical modeling parameters were investigated. The numerical methods generally showed good agreement with each other, except at some transonic Mach numbers. Both methods showed good to excellent agreement with experimental data in the high transonic and supersonic Mach regimes. In the subsonic and low transonic regimes, agreement between numerical and experimental data was less favorable. The accuracy of the free-flight test data in these regimes was uncertain due to instances of large scatter, large standard deviation errors and different data sources showing significantly different results.

15. SUBJECT TERMS

computational fluid dynamics, dynamic stability derivatives, pitch damping, projectiles

16. SECURITY CLASSIFICATION OF:			17. LIMITATION OF ABSTRACT	18. NUMBER OF PAGES	19a. NAME OF RESPONSIBLE PERSON Vishal A. Bhagwandin
a. REPORT	b. ABSTRACT	c. THIS PAGE			19b. TELEPHONE NUMBER *(Include area code)*
Unclassified	Unclassified	Unclassified	UU	52	410-306-0731

Standard Form 298 (Rev. 8/98)
Prescribed by ANSI Std. Z39.18

Contents

List of Figures

List of Tables

Acknowledgments

INTENTIONALLY LEFT BLANK.

1. Introduction

Aerodynamic prediction of dynamic stability derivatives is critical to the design of ballistic and missile weapons. Dynamic stability derivatives are a measure of how the in-flight forces and moments acting on a flight body change in response to changes in flight states, such as angle of attack and velocity. The main dynamic stability derivatives are the pitch damping force, pitch damping moment, roll damping moment, Magnus force and Magnus moment. These dynamic stability derivatives are used to conduct flight stability analyses as projectiles undergo complex pitch-roll-yaw motions. This ensures stable yet maneuverable airframe designs for precision projectile munitions.

Computational fluid dynamics (CFD) is recognized as an efficient and cost-effective tool for predicting aerodynamic forces and moments, and often complements free-flight ballistic range tests, wind-tunnel experiments, and semi-empirical analytical estimation. In this study, Reynolds-Averaged Navier−Stokes (RANS) CFD techniques and linear flight mechanics theory were used to compute the pitch damping force (PDF) and pitch damping moment (PDM) for a finned projectile using two methods, viz, the "transient planar pitching" method (*1−11*), and the "steady lunar coning" method (*12–21*). Most studies have independently used these two methods, but the methods were not directly compared, and were mostly applied to supersonic flight. DeSpirito et al (*11*) applied both methods to an axisymmetric spinner rocket, but not to a finned projectile. This study presents the first combined application of these methods for finned projectiles in which these methods were quantitatively assessed and directly compared for accuracy and efficiency in predicting the pitch damping dynamic stability derivatives across the full Mach number regime, viz, subsonic, transonic and supersonic. Detailed investigations were conducted for each method to determine modeling sensitivities and limitations with respect to numerical and aerodynamic modeling parameters. These included the effect of fin cant and computational grid density on the numerical solutions.

Transient planar pitching (PP), for the purpose of this study, is the motion whereby the projectile harmonically oscillates about its center of gravity in rectilinear flight. This is numerically achieved via a forced sinusoidal motion. This motion is time-dependent, and therefore time-accurate CFD methods were used to compute the flow solution. Linear mechanics theory relates the pitch damping force and moment (PDF/M) to the normal force and pitching moment as the projectile oscillates, allowing the PDF/M to be calculated (*22–24*). In addition to the effect of fin cant and grid density, investigations included dependence on the timestep and inner iterations of the RANS time integration scheme, and dependence on the oscillation amplitude and frequency.

Steady lunar coning (LC) is the motion whereby the projectile flies at a constant angle with respect to the freestream velocity vector while undergoing a constant angular rotation about a line parallel to the freestream velocity vector and passing through the projectile's center of

gravity. This coning motion is comprised of two time-dependent orthogonal pitching motions plus a time-dependent spinning motion. However, the combination of these motions is time-independent, allowing the use of steady-state (SS) CFD methods to compute the flow solution (*20*). Linear mechanics theory (*15*, *19*) relates the PDF/M to the side force and moment, side force, and moment angle of attack derivatives, and the Magnus force and moment derivatives during the coning motion, allowing the PDF/M to be calculated. Previous studies have assumed the Magnus force and moment to be negligible for finned projectiles undergoing lunar coning motion (*16*, *20*) resulting in approximated pitch damping solutions. This study computed the Magnus components of lunar coning via separate transient axial roll simulations to theoretically obtain more accurate pitch damping force and moment predictions. In addition to the effect of fin cant and grid density, investigations included dependence on the coning rate and coning angle.

The projectile flowfields for the prescribed dynamic motions were computed using CFD++ (*25*), a commercial fluid flow solver by Metacomp Technologies. The three-dimensional, compressible RANS equations of fluid dynamics were solved, from which the aerodynamic forces, moments and stability derivatives were calculated.

The computations were performed for two basic finned projectiles, viz, the Army-Navy Basic Finner (ANF) and the Air Force Modified Finner (AFF). These projectiles have been used as reference projectiles for many years and have been extensively tested in aeroballistic free-flight ranges and wind tunnels (*26*–*29*). Data were obtained for validation of CFD results from experiments conducted at Defense Research and Development Canada (DRDC) Valcartier Aeroballistic Range and Trisonic Wind-Tunnel Facilities (*26*–*28*) in Quebec, Canada, and the U.S. Air Force Research Laboratory (AFRL) Aeroballistic Research Facility (ARF) (*29*) at Eglin Air Force Base in Florida.

2. Theoretical Basis

The total forces and moments acting on the projectile with respect to (w.r.t.) the projectile-fixed coordinate reference frame were obtained from the RANS solution. These total forces and moments were nondimensionalized using freestream density, freestream velocity, and a reference area—the cross-sectional area of the projectile at the center of gravity location—to obtain the total force and moment coefficients (standard aerodynamic procedures). The data were then manipulated using linear flight mechanics theory to compute the PDF/M dynamic stability derivatives, defined as (*22*–*23*)

$$\text{PDF/M} = \frac{1}{2}\rho V^2 S\left[\left(\frac{qD}{2V_\infty}\right)C_{j_q} + \left(\frac{\dot{\alpha}D}{2V_\infty}\right)C_{j_{\dot{\alpha}}}\right] \text{ for } j = N, m \tag{1}$$

where q and $\dot{\alpha}$ are the pitch rate and angle of attack rate (also called the plunge rate), respectively. C_{j_q} and $C_{j_{\dot{\alpha}}}$ are pitch and plunge derivative coefficients, respectively. Because it is usually difficult to experimentally and numerically compute the individual components C_{j_q} and $C_{j_{\dot{\alpha}}}$, the coefficient sum $\left[C_{j_q} + C_{j_{\dot{\alpha}}} \right]$ is instead computed; this is consistent with current practice. The terms "PDF/M" and "PDF/M sum" are therefore used interchangeably in the remainder of this report.

The pitch damping force is often small in comparison to the pitch damping moment and is therefore often neglected. In fact, there were no pitch damping force experimental data to compare to in this study. However, CFD pitch damping force results are still presented herein for completeness. The pitch damping moment can have a significant impact on stability and should be negative for dynamically stable flight.

The following sections describe how the PDF/M coefficients were obtained using two different methods, viz, (1) transient planar pitching and (2) steady lunar coning. All forces and moments were measured w.r.t. the projectile-fixed coordinate system whose x-axis is positive "nose-to-tail," z-axis is positive "up" and whose origin is at the center of gravity of the projectile.

2.1 Transient Planar Pitching Method

Transient planar pitching (also referred to as the forced planar pitching or forced oscillation method) is the motion whereby the projectile harmonically oscillates about its center of gravity in rectilinear flight. This motion is time-dependent and requires time-accurate/unsteady RANS to numerically compute the flow solution. For this motion, first-order Taylor series expansion of in-plane forces and moments, represented by C_j as a function of time, t, results in (*22–24*)

$$C_j(t) = C_{j_0} + C_{j_\alpha}\alpha(t) + C_{j_q}\frac{q(t)D}{2V_\infty} + C_{j_{\dot{\alpha}}}\frac{\dot{\alpha}(t)D}{2V_\infty}, \quad j = N, m \tag{2}$$

where C_{j_0} is the zero-angle of attack static coefficient and C_{j_α} is the angle of attack derivative coefficient.

Forced planar pitching is numerically achieved by imposing a small-amplitude oscillation about a mean angle of attack, α_0, defined by the sinusoidal function

$$\alpha(t) = \alpha_0 + A\, sin(\omega t) \tag{3}$$

where A is the amplitude of the pitching motion (typically <1°), ω is the angular velocity, and α is the pitch angle relative to the body-fixed reference frame at time t. For this study, the PDF/M were computed at zero angle of attack, therefore α_0=0. For forced planar pitching, the pitch rate and angle of attack rate are equal, that is

$$q = \dot{\alpha} \tag{4}$$

For simplification, and consistency with current literature, a reduced pitch frequency, k, is defined as

$$k = \frac{\omega D}{2V_\infty} \tag{5}$$

The PDF/M can be calculated via two approaches as described below.

2.1.1 Approach I: Integrating Over a Period of Oscillation

This approach is more generalized and has been used by Park et al. (6, 7) and McGowan et al. (3), among others. For small amplitude oscillation, the PDF/M can be assumed constant. Integrating equation 2 w.r.t. α, and combining with equation 4, yields

$$C_{j_q} + C_{j_{\dot{\alpha}}} = \frac{2V_\infty}{D} \frac{\int \left[C_j(t) - C_{j_0} - C_{j_\alpha}\alpha(t) \right] d\alpha}{\int \dot{\alpha}(t) d\alpha} \tag{6}$$

The integrals of C_{j_0} and C_{j_α} over one period of motion is zero, and equation 6 simplifies to

$$C_{j_q} + C_{j_{\dot{\alpha}}} = \frac{2V_\infty}{D} \frac{\int C_j(t) d\alpha}{\int \dot{\alpha}(t) d\alpha} \tag{7}$$

Substituting equations 3 and 5 into equation 7, the following is obtained for the PDF/M

$$\text{PDF/M} = C_{j_q} + C_{j_{\dot{\alpha}}} = \frac{2V_\infty}{\pi AD} \int_0^T C_j(t) \cos\left(\frac{2V_\infty k}{D}t\right) dt, \quad j = N, m \tag{8}$$

The variation of C_j with time over a period of oscillation is obtained from the RANS simulation, and the integral in equation 8 can be solved using the trapezoidal rule, as follows:

$$\int_0^T f(t) \, dt = \frac{1}{2}\sum_{n=1}^{N-1}[(t_{n+1} - t_n)] \, [f(t_{n+1}) + f(t_n)] \tag{9}$$

where

$$f(t) = C_j(t) \cos\left(\frac{2V_\infty k}{D}t\right) \tag{10}$$

and N is the number of numerical timesteps per period of oscillation used for solving the RANS equations.

2.1.2 Approach II: Solving at the Mean Angular Displacement Position

This approach has been used by Sahu (8), DeSpirito et al. (11) and Bhagwandin et al. (1, 2), among others, for generic projectile and missile configurations. Figure 1 shows a sample pitching moment history (a similar plot can be shown for the normal force history) about a mean angle of attack $\alpha_0 = 30°$ for the ANF. The forced oscillation produces a hysteresis variation with α. For most munition projectiles, this variation is quasi-steady and symmetric about α_0. The

PDF/M can thus be computed using just the two points during an oscillation where the projectile passes through α_0. Let the subscripts "+" and "−" represent the pitch-up and pitch-down motions, respectively. Then, evaluating equations 2–5 at $\alpha = \alpha_0$ results in

$$\left[C_{j_q} + C_{j_{\dot{\alpha}}} \right]_{\alpha=\alpha_0} = (-1)^n \frac{\left(C_{j\pm} - C_{j_0} - C_{j_\alpha}\alpha_0 \right)}{kA}, \quad n = 0, 1, 2, 3, \dots \tag{11}$$

where n represents every half oscillation, and $C_{j\pm}$ is the value of C_j when $\alpha = \alpha_0$. equation 11 can be used to calculate the PDF/M, where C_{j_0} and C_{j_α} can be determined via a steady-state static RANS solution at $\alpha=\alpha_0$. However, the symmetric nature of the pitch-up and pitch-down motions leads to the following simplification:

$$\text{PDF/M} = \left[C_{j_q} + C_{j_{\dot{\alpha}}} \right]_{\alpha_0} = \frac{C_{j+} - C_{j-}}{2kA}, \quad j = N, m \tag{12}$$
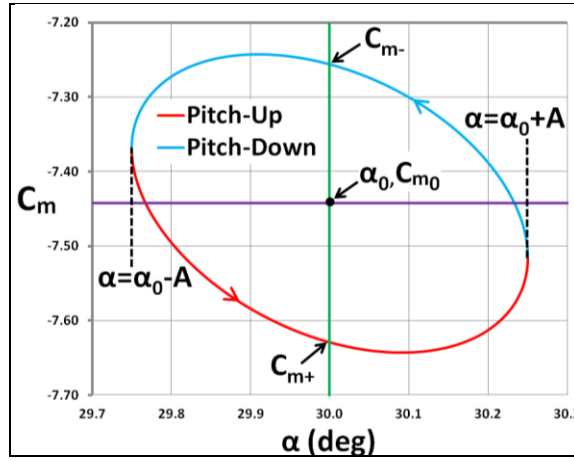
Figure 1. Sample pitching moment history as a
function of angle of attack for $\alpha_0 = 30°$.

For the planar pitching motion, the nominal chosen pitch amplitude, A, was $0.25°$ and reduced pitch frequency, k, was 0.1. The formulations in both approaches imply that the normal force and pitching moment must vary linearly with A and k. This linear dependence was investigated at sample Mach numbers of 0.9 and 4.5, the results of which are presented in section 4.2.3. The pitch frequency, f, and period of oscillation, T, can be calculated from

$$f = \frac{1}{T} = \frac{V_\infty k}{\pi D} \tag{13}$$

The nominal number of integration timesteps per oscillation, N, used to solve the RANS equations was 200. The numerical integration timestep, Δt, (also referred to as the global or physical timestep) was therefore determined as

5

$$\Delta t = \frac{T}{N} = \frac{\pi D}{N V_\infty k} \tag{14}$$

Several values of N were tested to determine its effect on numerical convergence, the results of which are presented in section 4.2.2.

2.2 Steady Lunar Coning Method

Murphy (*24*), Schiff (*15, 16*), Tobak and Schiff (*17, 18*) and Tobak et al (*19*) have theoretically examined the aerodynamics of bodies undergoing coning motion. Weinacht et al (*20–21*), among others, later applied Navier−Stokes numerical techniques to solve the flowfield of projectiles undergoing coning motion in order to calculate the PDF/M. For the purpose of this study, steady coning is the motion whereby the projectile flies at a constant angle, α, with respect to the freestream velocity vector while undergoing a constant angular rotation, $\dot{\phi}$, about a line parallel to the freestream velocity vector and passing through the projectile's center of gravity. In this case, α is therefore the total angle of attack, that is, the magnitude of the vector sum of the vertical and horizontal angles of attack. This coning motion is a comprised of two time-dependent orthogonal pitching motions plus a time-dependent spinning motion. However, the combination of these motions is time-independent, allowing the use of steady-state RANS to numerically compute the flow solution (*20*). For this coning motion, as derived from the general case of arbitrary motion (*14*), the side moment, C_n, is related to the Magnus moment derivative, $C_{n_{p\alpha}}$, pitch damping moment sum, $C_{m_q} + C_{m_{\dot{\alpha}}}$, and the side moment angle of attack derivative, C_{n_α}, as follows (*20–21*):

$$C_n = \sigma \frac{\dot{\phi} D}{2V} \left(\gamma C_{n_{p\alpha}} + \left[C_{m_q} + \gamma C_{m_{\dot{\alpha}}} \right] \right) + \sigma C_{n_\alpha} \tag{15}$$

A nondimensional angular coning rate, Ω, can be defined as

$$\Omega = \frac{\dot{\phi} D}{2V_\infty} \tag{16}$$

From equations 15 and 16, for linear variations of C_n with Ω

$$C_{n_{\dot{\phi}}} \equiv \frac{\partial C_n}{\partial \Omega} = \frac{C_n - \sigma C_{n_\alpha}}{\Omega} = \sigma \left(\gamma C_{n_{p\alpha}} + \left[C_{m_q} + \gamma C_{m_{\dot{\alpha}}} \right] \right) \tag{17}$$

For small coning angles, $\gamma = \cos \alpha \approx 1$. Therefore, from equation 17, the PDM coefficient sum can be expressed as

$$\text{PDM} = \left[C_{m_q} + C_{m_{\dot{\alpha}}} \right] = \frac{C_n - \sigma C_{n_\alpha}}{\sigma \Omega} - C_{n_{p\alpha}} \tag{18}$$

As stated, equation 17 assumes that C_n varies linearly with Ω. To satisfy this linear assumption, several coning rates were tested for select Mach numbers, the results of which are presented in section 4.3.2. For a symmetric finned projectile without fin cants or bevels, $C_n = 0$ when $\Omega = 0$, and only a single coning computation at some nonzero Ω within the linear range is required to compute $\partial C_n / \partial \Omega$. For a finned projectile with fin cants or bevels, since $C_n \neq 0$, then simulations at two independent coning rates (which may include zero coning rate) are required to determine $\partial C_n / \partial \Omega$ (*20*).

The formulation in equation 18 also indicates that the PDM is independent of the coning angle for linear variations of $C_{n_{\dot\phi}} = \partial C_n / \partial \Omega$ with σ. The limits of this linear dependence were investigated using several coning angles at select Mach numbers, the results of which are also presented in section 4.3.2. The side force, C_Y, due to the coning motion can also be derived from the general case of arbitrary motion as (*20–21*)

$$C_Y = \sigma \frac{\dot\phi D}{2V} \left(\gamma C_{Y_{p\alpha}} + \left[C_{N_q} + \gamma C_{N_{\dot\alpha}} \right] \right) + \sigma C_{Y_\alpha} \tag{19}$$

By similar deduction, the PDF coefficient sum can be derived as

$$\text{PDF} = \left[C_{N_q} + C_{N_{\dot\alpha}} \right] = \frac{C_Y - \sigma C_{Y_\alpha}}{\sigma \Omega} - C_{Y_{p\alpha}} \tag{20}$$

2.2.1 Transient Roll

The Magnus force and moment that arises during coning results from unequal fluid pressures on opposite sides of the projectile body. The Magnus force and moment derivatives, $C_{Y_{p\alpha}}$ and $C_{n_{p\alpha}}$, cannot be determined directly from the coning simulation. Because the Magnus effect arises only from the spin component of the coning motion, then a separate "transient rolling" simulation was performed. Rolling, in this case, is the motion whereby the projectile flies at a constant angle, α, with respect to the freestream vector while rotating about its body-fixed x-axis with constant angular velocity, p. This time-dependent spinning motion is intended to replicate the spin component of the coning motion. Therefore, the rolling motion was executed such that (*20*)

$$\alpha_{roll} = \alpha_{cone} \tag{21}$$

$$p = \gamma \dot\phi = \gamma \frac{2V_\infty \Omega}{D} \tag{22}$$

This method is not discussed or investigated in as much detail as the previous methods. It is only used to quantify the Magnus effect during coning. A future study will utilize this method to compute the roll damping stability derivatives and Magnus effect, where more detailed investigations will be provided.

For the rolling simulations, the projectile was spun for two full rotations completing 720° using a nominal $N = 1440$ numerical timesteps per rotation [based on tested values in references (*8, 30*)], equivalent to spinning the projectile 0.25° every timestep. The timestep, Δt, was therefore computed as

$$\Delta t = \frac{T}{N} = \frac{2\pi}{Np} \tag{23}$$

where T is the period of rotation. The side force and moment, C_Y and C_n, were then averaged from the final rotation. Assuming a linear variation of C_Y and C_n with Ω and α, then the Magnus force and moment derivatives, $C_{Y_{p\alpha}}$ and $C_{n_{p\alpha}}$, were computed as

$$C_{Y_{p\alpha}} = \frac{C_Y - C_{Y_0}}{\sigma\Omega} \tag{24}$$

$$C_{n_{p\alpha}} = \frac{C_n - C_{n_0}}{\sigma\Omega} \tag{25}$$

where C_{Y_0} and C_{n_0} are the side force and moment, respectively, at zero spin rate and are mainly due to fin cants/bevels. C_{Y_0} and C_{n_0} were computed via separate steady-state RANS simulations. The Magnus force and moment computed via equations 24 and 25 should be the equivalent Magnus force and moment generated during the coning motion, and are thus substituted into equations 20 and 18, respectively.

3. Geometry and Computational Methodology

3.1   Projectile Configurations and Experimental Data

Two finned projectiles were used as test models, viz, the ANF and the AFF. Figure 2 shows the geometry details of the ANF. The ANF had a diameter of 0.03 m (1 caliber), and consisted of a 10° cone that was 2.84 calibers long, followed by a 7.16 caliber cylindrical body. There were four 1×1 caliber fins with sharp leading edges and thicknesses of 0.08 calibers at the trailing edge. CFD data for fin cants of $\delta = 0°$ (baseline case) and $\delta = 2°$ were used for comparison with experiment. The center of gravity of the ANF was located 5.5 calibers from the nose tip. The mass of the model was 1.5894 kg. The axial and transverse moments of inertia were 1.924×10^{-4} kg·m^2 and 9.874×10^{-3} kg·m^2, respectively.
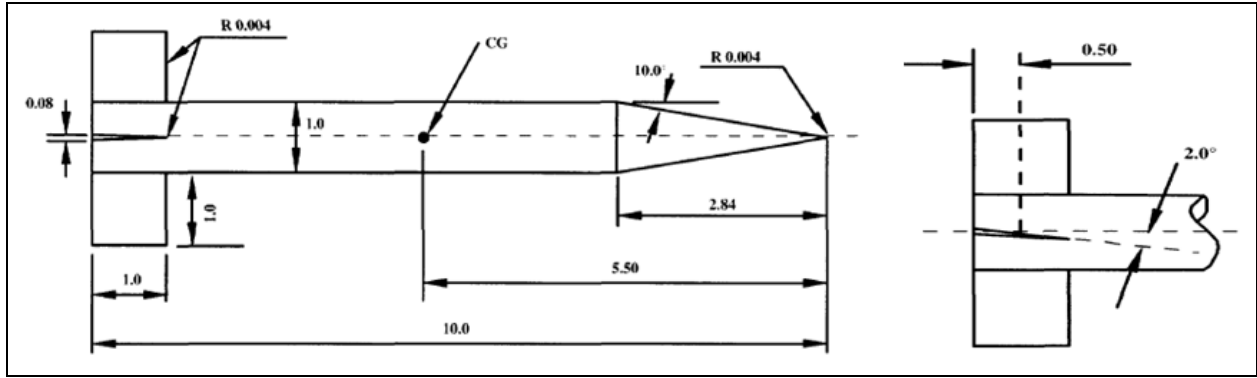
Figure 2. ANF (*27*), dimensions in calibers, one caliber = 0.03 m.

Figure 3 shows the geometry details of the AFF. The AFF also had a diameter of 0.03 m (one caliber) and consisted of tangent ogive nose that was 2.5 calibers long followed by 7.5 caliber cylindrical body. There were four clipped-delta fins with sharp leading and trailing edges. Although canted fin data were available, only the 0° fin cant experimental data were used for comparison with CFD. The center of gravity of the AFF was located 4.8 calibers from the nose tip. The mass of the model was 0.6643 kg. The axial and transverse moments of inertia were 7.197×10^{-4} kg·m^2 and 4.857×10^{-3} kg·m^2, respectively.
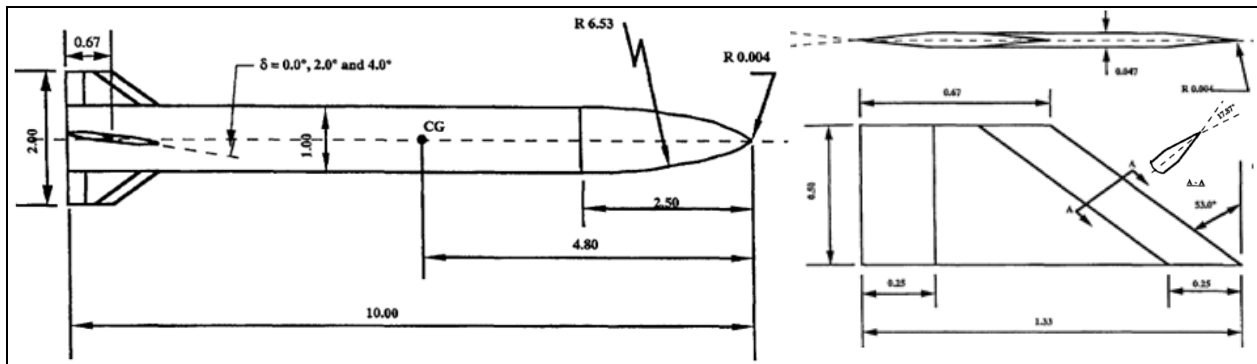
Figure 3. AFF (*28*), dimensions in calibers, one caliber = 0.03 m.

For comparison with CFD results, experimental data for both the ANF and AFF were obtained mainly from free-flight (FF) tests conducted at DRDC-Valcartier Aeroballistic Range (*26–28*). Nominal pressure and temperature flight conditions were $P_S = 01325$ Pa and $T_S = 293.15$ K, respectively. Test Mach numbers ranged from 0.5–4.5 for the ANF and 0.5–2.5 for the AFF. The Reynolds number, based on projectile length, ranged from 4.1×10^6 to 30.0×10^6. Models with fin cants of $\delta = 0$, 2, and 4° were also tested. The aerodynamic coefficients were reduced from the free-flight trajectory data (time, position, and orientation) using fixed-plane, six-degree-of-freedom (6-DOF) numerical integration analysis. Single-fit (SF) and multiple-fit (MF) data sets were obtained. The MF procedure simultaneously fits several flight data sets, including multiple fin cants, to a common set of aerodynamics to theoretically produce more

9

accurate aerodynamic coefficients. The quoted Mach number for each data set was the midrange Mach number for the SF data, and the average midrange Mach number for the multiple-fit data. For the moment aerodynamic coefficients, the moment reference center was located at the center of gravity of the projectile.

Additional static aerodynamic data for the ANF were also obtained from DRDC wind-tunnel (WT) tests (27). The wind-tunnel Reynolds number ranged from 1.4×10^6 to 2.9×10^6 for Mach numbers in the range 0.5–4.5. The static aerodynamic coefficients were obtained by least-square fitted polynomials through measured experimental data.

Additional experimental data for the AFF were obtained from free-flight tests conducted by AFRL ARF (29). The test model in this case was a scaled down version of the one used in the DRDC tests. The diameter of this model was 0.01905 m. The model was launched at atmospheric conditions similar to that of the DRDC tests at Mach numbers in the range 0.6–2.5. SF and MF aerodynamic coefficients were obtained by a similar reduction process as that used in the DRDC tests.

3.2 Computational Domains and Boundary Conditions

The baseline 0° fin cant computational grids for the ANF and AFF consisted of 17 and 15 M structured hexahedral cells, respectively, both constructed in Pointwise V16.03R4 (31) and both exported in double precision format (see figure 4). The grids were extended ~60 calibers in the radial direction to form spherical farfield boundaries, where a characteristics-based inflow/outflow boundary condition was applied. The first two cell layers from the farfield boundaries was set as absorbing layers, where a damping source term was added in CFD++ to prevent possible numerical wave reflections which may contaminate the flow solution. The projectile walls were designated viscous adiabatic walls and utilized a solve-to-the-wall strategy where the initial grid spacing normal to the walls was 0.0005 mm, satisfying the $y^+ \leq 1$ criteria for adequate boundary-layer resolution across all Mach numbers. A 20% stretching factor was used between successive grid points off the projectile walls. The 2° fin cant grid for the ANF was the same as that of the 0° fin cant grid, except for minor modifications near the fins to accommodate the fin cants.
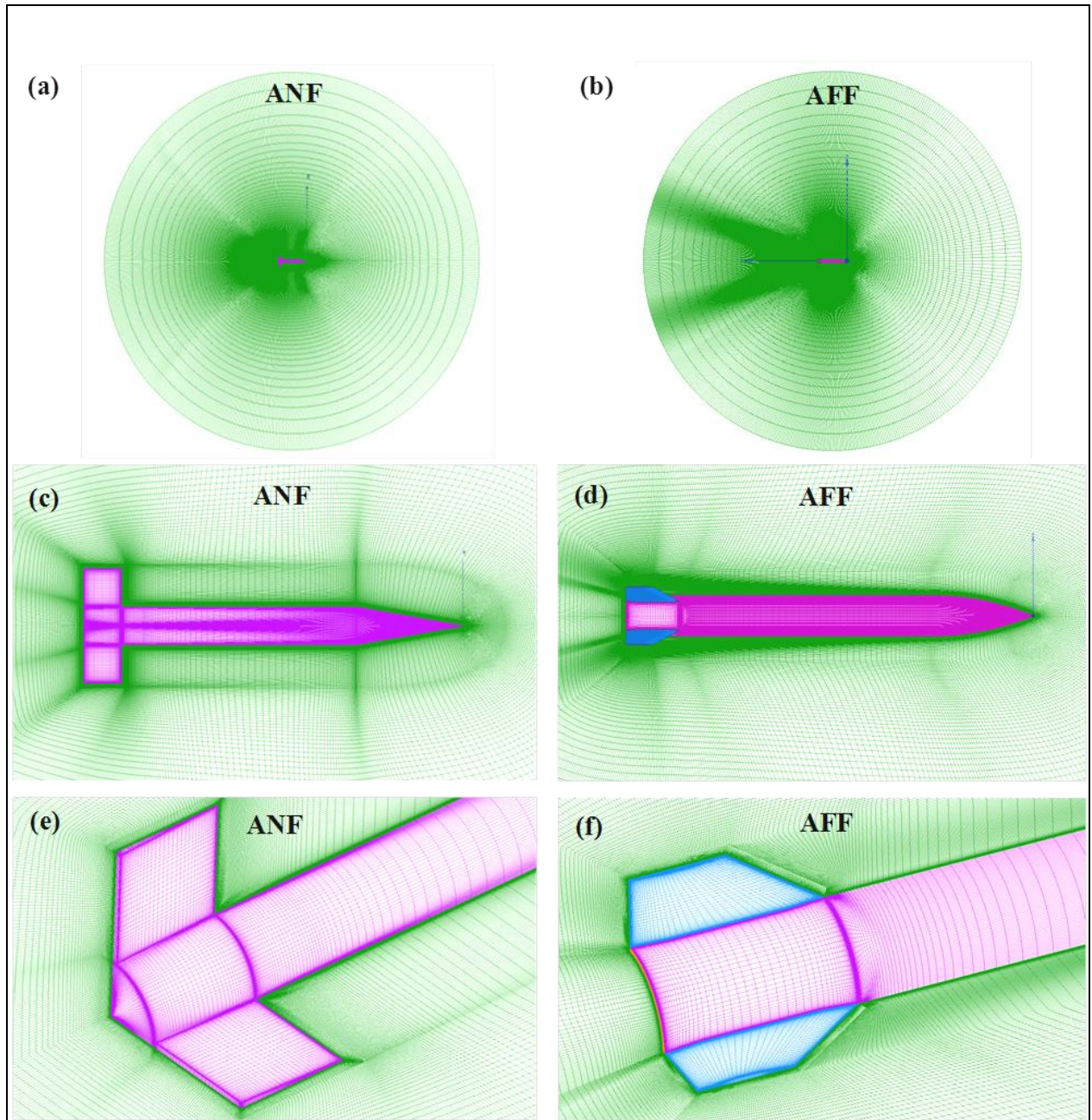
Figure 4. Computational grids ($\delta = 0°$) for ANF (left) and AFF (right): (a–b) whole grid on symmetry plane, (c–d) nearfield grid on symmetry plane and on projectile surface, and (e–f) grid detail between fins.

For the ANF projectile, dependence of the results on grid resolution was investigated using three grid levels at specific Mach numbers, viz, 0.5, 0.9, 1.1, 2.5, and 4.5. The aforementioned 17 M cell grid was the baseline grid and was labeled as the fine grid. The medium and coarse grids were obtained by reducing the number of grid points in each i, j, k direction by factors of 3/4 and 1/2, respectively. The resulting medium and coarse grids thus consisted of 6 M and 2 M cells, respectively. The initial grid spacings normal to the walls of the projectiles were increased by the same factors. For the AFF, only a single grid level was used.

The ANF and AFF grids were decomposed to facilitate parallel computation on 120 and 96 processors, respectively. The computations were performed on "Harold" – a SGI Altix ICE 8200 supercomputer consisting of 1344 compute nodes, 2 quad-core Intel Xeon Nehalems per node, 24 GB memory per node, and 4X DDR Infiniband interconnect. Harold is housed and managed by the ARL DOD Supercomputing Resource Center (ARL DSRC) at Aberdeen Proving Ground, Maryland.

3.3   Numerics

The flow solution at a given flight condition was computed using CFD++ v10.1 (*25*), a commercial CFD solver by Metacomp Technologies, Inc. CFD++ is a finite volume, unstructured solver capable of a wide range of aerospace applications and extensively used by ARL for projectile aerodynamic design and analysis. In this study, CFD++ was used to numerically solve the three-dimensional, compressible, RANS equations in order to compute the total aerodynamic forces and moments acting on the projectile, from which the static and pitch damping derivative coefficients were calculated. Double precision format was used for all computations. The following sections first describe general numerical attributes for the steady-state and time-accurate simulations, followed by a summary of the planar pitching, lunar coning, and rolling simulation procedures.

3.3.1 Steady-State Simulations

For all steady-state RANS simulations, the solution was advanced towards steady-state convergence using a point-implicit time integration scheme with local time-stepping, defined by the Courant−Friedrichs−Lewy (CFL) number. A linear ramping schedule was used to gradually increase the CFL over the first few hundred iterations, after which a constant CFL was maintained until convergence. The maximum CFL was usually between 10 and 100, depending on the freestream Mach number. The multigrid W-cycle method with a maximum of four cycles and a maximum of 20 coarse grid levels was used to accelerate convergence. Implicit temporal smoothing was applied for increased stability.

The spatial discretization function was a second-order, upwind scheme using a Harten−Lax−van Leer−Contact (HLLC) Riemann solver utilizing Metacomp's multi-dimensional Total-Variation-Diminishing (TVD) flux limiter. For freestream Mach numbers 1.5 and above, first-order spatial discretization was used for the first few hundred iterations, after which blending to second-order occurred over the next 100 iterations, and thereafter remained fully second-order.

The turbulence model employed was Metacomp's realizable k-ε model (*25*, *32*), which solves transport equations in conservative form for the turbulent kinetic energy (k) and turbulent dissipation rate (ε). The freestream turbulence intensity was set at 2% and the turbulent-to-laminar viscosity ratio at 50. Metacomp's wall-bounded compressibility correction was applied to realize diffusive mixing in the turbulent regions that would otherwise be underpredicted in compressible flows.

Reductions of five orders or more of the magnitudes of the cell-averaged residuals of the RANS equations were typically achieved within a few hundred iterations (for lower Mach numbers) to a few thousand iterations (for higher Mach numbers). However, the total force and moment coefficients converged relatively faster, usually within a few hundred iterations. Some cases did demonstrate relatively small pseudo-steady oscillations in the total aerodynamic coefficients. Therefore, for all steady-state cases, the coefficients were averaged over the final 100–200 iterations.

3.3.2 Time-Accurate Simulations

For the time-accurate/unsteady RANS simulations, the dual-time step method was employed with the point-implicit time integration scheme, utilizing an outer/physical/global timestep and an inner timestep. The inner timestep is a local nonphysical timestep used to converge the RANS equations at each physical timestep. For the inner iterations, the multigrid W-cycle method and implicit temporal smoothing was applied. Nominally, $i = 20$ inner timesteps were used for the time-accurate simulations, usually resulting in 0.5–1 order of magnitude reduction in the cell-averaged "inner" residuals of the RANS equations. Other values were tested for convergence, the results of which are presented in section 4. The spatial discretization scheme and turbulence model used in the time-accurate simulations were the same as that used in the steady-state simulations.

3.3.3 Transient Planar Pitching Procedure

First, a static steady-state solution at a given Mach number was generated at an angle of attack $\alpha = \alpha_0 = 0°$. This steady-state solution was then used as the initial condition for the time-accurate planar pitching simulation. The planar pitching oscillation was defined by the sinusoidal function in equation 3 about a mean angle of attack $\alpha_0 = 0°$ with a chosen nominal amplitude and reduced frequency of $A = 0.25°$ and $k = 0.1$, respectively. A total of three oscillations/pitch cycles were run with a nominal $N = 200$ timesteps per oscillation. Initial numerical transients were typically mitigated well within the first oscillation, after which a quasi-steady cyclical convergence of the in-plane total forces and moments was obtained. The histories of the total normal force and pitching moment coefficients, C_N and C_m, for the final two oscillations were used to determine the PDF/M using equation 8 for approach I, and equation 12 for approach II, respectively (see section 2.1).

3.3.4 Steady-State Lunar Coning Procedure

With the velocity vector parallel to the inertial x-axis, the projectile (and grid) was rotated to the nominal coning angle $\alpha = 0.5°$. The projectile was then made to rotate about an axis parallel to the velocity vector and passing through the projectile's center of gravity at a constant angular velocity, $\dot{\phi}$, calculated based on a chosen nominal nondimensional coning rate of $\Omega = 0.0025$. The steady-state converged values of the total side force and moment coefficients, C_Y and C_n, were then used to compute the PDF/M via equations 20 and 18, respectively. For the 2° canted

fin ANF, the side force and moment α-derivative coefficients, C_{Y_α} and C_{n_α}, were calculated from steady-static simulations at $\alpha = 0°$ and $0.5°$. The Magnus terms in these equations were obtained from the transient rolling simulations, described below.

3.3.5 Transient Rolling Procedure

The objective of the rolling simulations was to obtain the equivalent Magnus force and moment acting on the projectile due to the spin component of the coning motion. Because the nominal coning angle was $\alpha = 0.5°$, the steady-state static solution at $\alpha = 0.5°$ was thus used as the initial condition for the transient rolling simulations. For the rolling simulations, the projectile was made to rotate about its body-fixed x-axis at angle of attack, α, w.r.t. the freestream velocity vector with constant angular velocity, p, such that equations 21 and 22 were satisfied. The projectile was spun for two rotations completing $720°$ or $4\pi^{\mathrm{c}}$. Initial numerical transients were typically mitigated well within the first rotation. The total side force and moment coefficients, C_Y and C_n, were averaged over the final rotation. The Magnus force and moment coefficients, $C_{Y_{p\alpha}}$ and $C_{n_{p\alpha}}$, were then computed via equations 24 and 25, respectively. For the 2° canted fin ANF, the zero-spin side force and moment coefficients, C_{Y_0} and C_{n_0}, were obtained from the steady-state static simulations at $\alpha = 0.5°$.

4. Results

Section 4.1 briefly presents results for prediction of static aerodynamic coefficients for the ANF and AFF. Sections 4.2 and 4.3 show the dependence of the planar pitching and lunar coning methods, respectively, on various numerical and physical modeling parameters. These parametric studies were conducted only on the ANF and only for the PDM. The PDF is often ignored in aerodynamic analyses since it does not affect flight stability. In fact, there were no experimental data to compare to for the PDF. For these reasons, all PDF results are deferred to section 4.4. Section 4.4 finally compares the planar pitching and lunar coning methods for both the ANF and AFF.

4.1 Steady-state Static Results for ANF and AFF

Figure 5 compares the static aerodynamic coefficients, viz, the axial force, normal force slope, and pitching moment slope coefficients at zero angle of attack, that is, C_{X0}, $C_{N_{\alpha_0}}$ and $C_{m_{\alpha_0}}$, for Mach numbers in the range 0.5–4.5. $C_{N_{\alpha_0}}$ and $C_{m_{\alpha_0}}$ were calculated using a linear fit between steady-state static solutions at 0 and 1° angles of attack. This is consistent with current practice because these coefficients tend to vary linearly at low angles of attack. Although these coefficients were not required for computing the pitch damping coefficients, they serve as a check of accuracy of the static steady-state RANS solutions, which were used as initial conditions for the dynamic time-accurate simulations. The CFD numerical data generally show

14

excellent agreement with free-flight and wind-tunnel tests across the full Mach number regime; for the ANF the agreement is slightly better with the free-flight data than with the wind-tunnel data at some Mach numbers. CFD data for the 2° canted fin ANF are also shown. There is no significant difference between the canted and uncanted results. This is expected because these coefficients do not typically vary with fin cant.
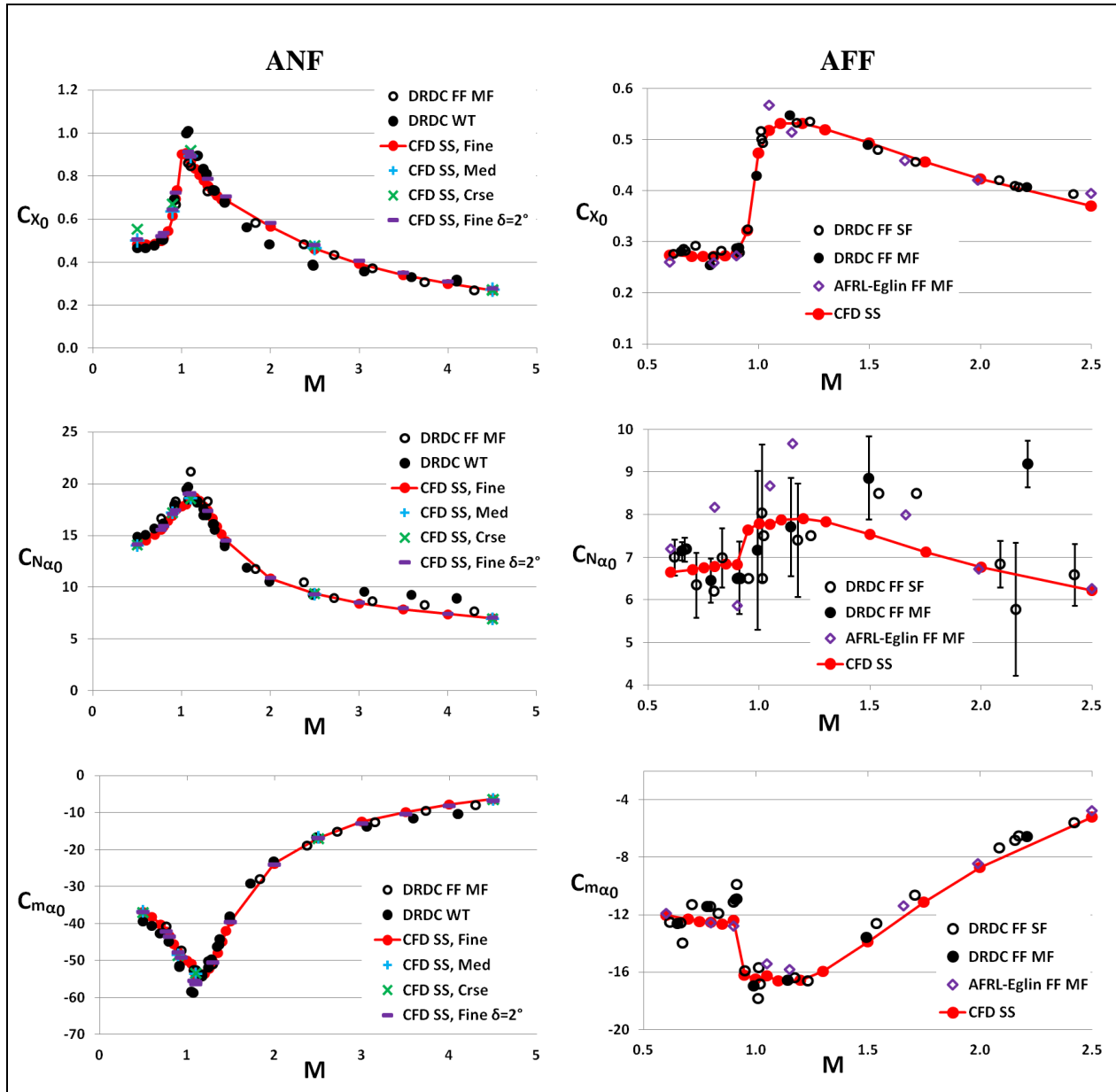

Figure 5. Static coefficient prediction at zero angle of attack as a function of Mach number for the ANF (left) and AFF (right). Shown here are axial force (C_{X_0}), normal force derivative ($C_{N_{\alpha_0}}$), and pitching moment derivative ($C_{m_{\alpha_0}}$) coefficients at zero angle of attack.

The $C_{N_{\alpha_0}}$ experimental data for the AFF, however, show much scatter. The DRDC standard deviation errors for this coefficient were much higher than that of the other coefficients. Supersonically, although the DRDC single-fit and AFRL multiple-fit data match reasonably well, the DRDC multiple-fit data are predicted to be much higher at Mach 2.2. According to DRDC, the source of this discrepancy is undetermined. The CFD data appear to pass through the average of the experimental data points up to Mach 1.2, then slightly underpredicted between Mach 1.2 and 2.0; then at Mach 2.0 and 2.5 there is excellent agreement with the DRDC single-fit and AFRL multiple fit data points. Because the CFD predictions of $C_{m_{\alpha_0}}$ for the AFF are in good agreement with experiment, then this is usually an indication that the CFD predictions of $C_{N_{\alpha_0}}$ is also good. It is likely therefore that the DRDC multiple-fit data for the AFF are incorrect.

Figure 5 also compares the effect of grid resolution on static coefficient prediction for the ANF at specific Mach numbers, viz, 0.5, 0.9, 1.1, 2.5, and 4.5. Three grid levels were compared, viz, fine, medium, and coarse, as previously discussed. Figure 5 shows that the results are relatively grid-independent, except for some small differences in the subsonic/transonic region for C_{X_0}, where the difference reaches a maximum of 14% at Mach 0.5. Overall, the fine grid was deemed to be adequate for grid independent solutions, and was thus retained as the baseline grid.

Figure 6 provides a synopsis of typical static steady-state flowfields for the ANF and AFF at zero angle of attack. Shown are Mach number contours on the symmetry plane at representative freestream Mach numbers of 0.9 and 2.0. Typical flow features are observed, such as the formation of shock waves on the nose and fins and low speed flows at the base of the projectiles.
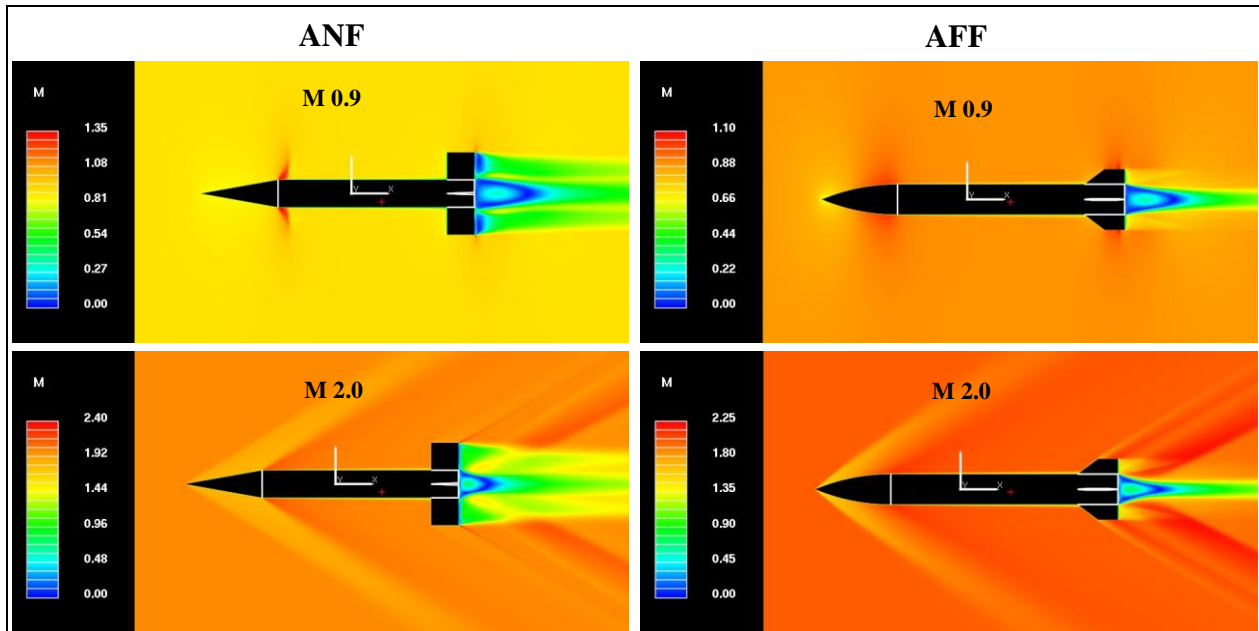
Figure 6. Mach number numerical flowfield on *x-z* symmetry plane for the ANF (left) and AFF (right). Results are from steady-state static simulations at $\alpha = 0$.

4.2   Transient Planar Pitching Parameter Study for the ANF

4.2.1 General Trend, Grid Dependence and Effect of Fin Cant

Figure 7 shows the PDM sum, $C_{m_q} + C_{m_{\dot\alpha}}$, for Mach numbers in the range 0.5–4.5 computed via the planar pitching simulations. Two approaches were described in section 2.1 for postprocessing the CFD data to calculate the PDF/M. Approach I (using integration over a period of oscillation, represented by the dashed green circles) and approach II (using two points in time at the average angular displacement position, represented by the red circles/red line) compare almost exactly in figure 7. Because the latter approach is simpler, it was used for all remaining calculations of the PDF/M using the planar pitching method for both the ANF and AFF.
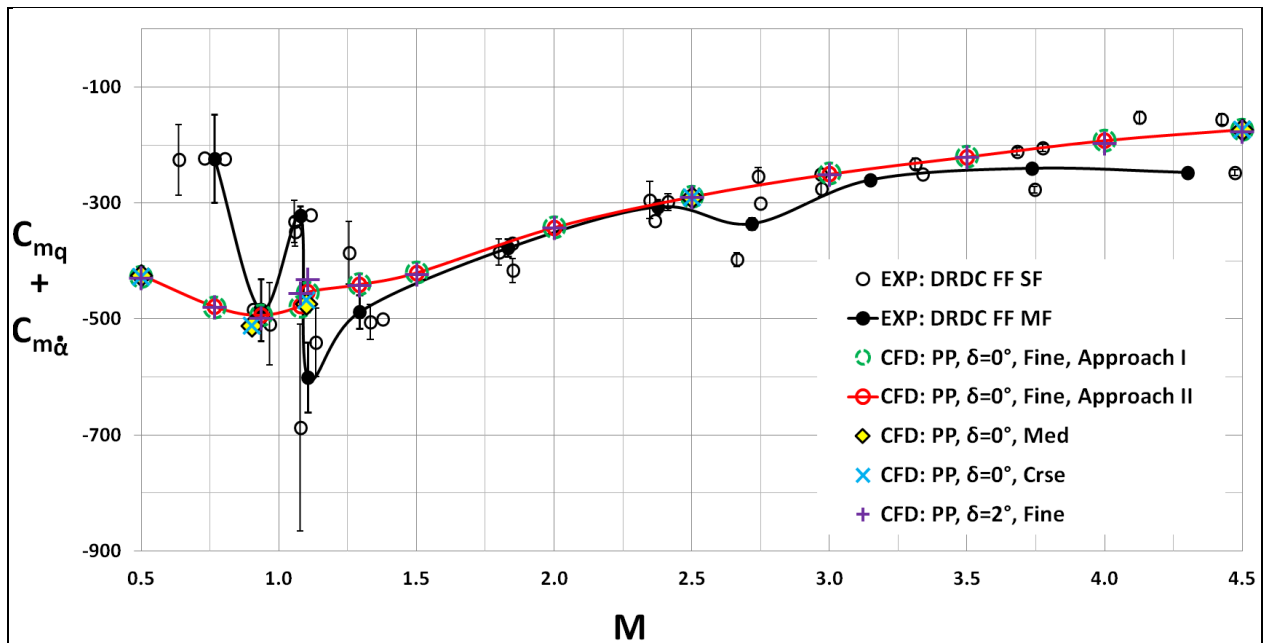
Figure 7. PDM as a function of Mach number, ANF planar pitching parameter study.

The coarse, medium and fine (baseline) grid results show excellent agreement at Mach 0.5, 0.9, 1.1, 2.5, and 4.5 (see figure 7 and table 1). The maximum percent differences occur at Mach 1.1 reaching 2.3% for the PDM between the fine and medium grids. The results indicate that the coarse grid may have provided adequate accuracy for PDF/M predictions using the planar pitching method. However, most simulations were performed prior to the grid resolution study. As a result, the fine grid was retained as the baseline grid.

Table 1. Planar pitching predictions: percent differences between grid levels for ANF.

Mach No.	Planar Pitching			
	Difference Between Fine and Medium Grids		Difference Between Fine and Coarse Grids	
	PDF (%)	PDM (%)	PDF (%)	PDM (%)
0.5	0.01	0.09	0.51	0.76
0.9	0.03	0.01	0.08	0.01
1.1	1.82	2.28	0.63	0.92
2.5	0.02	0.14	0.14	0.42
4.5	0.45	0.03	0.18	0.21

Figure 7 shows no significant difference between the canted fin ($\delta = 2°$) and uncanted fin ($\delta = 0°$) numerical results, except near Mach 1.0 where the difference reaches about 5%.

Compared to DRDC free-flight data, the PDM CFD data are about 115% larger in magnitude at Mach 0.766 (first free-flight multiple-fit data point in figure 7). Through the transonic region, $0.9 < M < 1.3$, there is much scatter in the free-flight data with very large standard deviation errors in the vicinity of Mach 1.0. In this region, the CFD PDM data appear to pass through the average of the experimental data points. The accuracy of the free-flight data in the subsonic and transonic regions is suspect, especially when multiple experimental data sources for the AFF are compared later in section 4.4. Additional test data would be required to determine the accuracy of the CFD predictions in this region. Above Mach 1.3, the CFD data generally show very good agreement with the free-flight data.

4.2.2 Inner Iteration and Timestep Dependence

The planar pitching simulations were time-dependent. As previously discussed, the dual-timestep method was used where the physical/global timestep, Δt, was calculated based on a chosen N=200 timesteps per oscillation, and the inner timestep was calculated based on a chosen $i = 20$ inner iterations per global iteration. Figures 8 and 9 show the effect of increasing i and N, respectively. This study was performed only for the ANF at representative freestream Mach numbers of 0.9 and 4.5. For these cases, the amplitude and reduced frequency of the oscillations were $A = 0.25°$ and $k = 0.1$, respectively (the baseline values).

Varying i from 5–25 in increments of 5, figure 8 shows that the PDM for the Mach 0.9 solutions readily converge by $i = 10$ for both $N = 100$ and 200. For the Mach 4.5 cases, the PDM shows an asymptotic convergence, where for $i > 15$ the PDM successively decreases by only ~1%. For consistency and accuracy, $i = 20$ was thus chosen as the nominal number of inner iterations at all Mach numbers.

Varying N from 100–400, the PDM shows asymptotic decrease in figure 9. For $i = 20$, increasing N from 200 to 400 decreased the PDM by only 1.5% at Mach 0.9 and 2% at Mach 4.5. Thus, sacrificing only little accuracy for a large gain in computing efficiency, $N = 200$ was deemed a reasonable nominal choice at all Mach numbers.
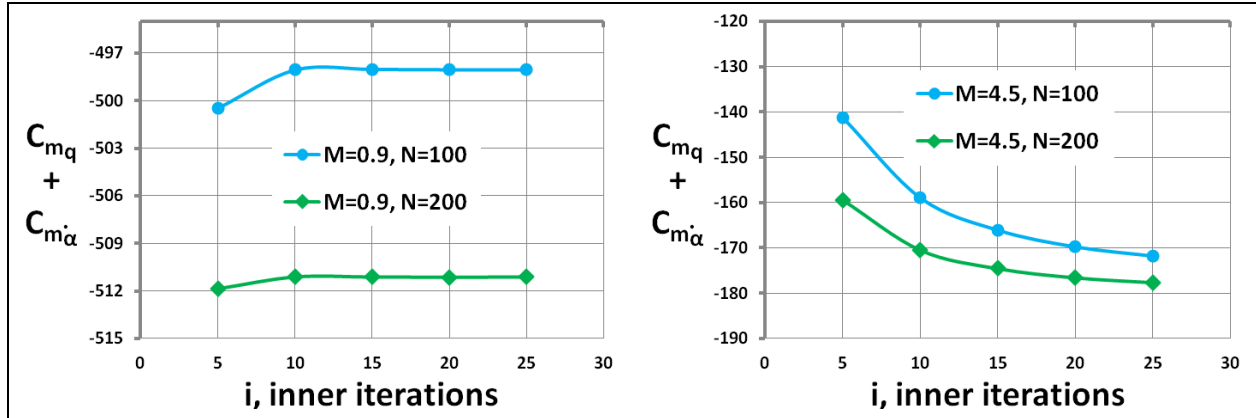
Figure 8. Effect of inner iterations on PDM at Mach 0.9 (left) and Mach 4.5 (right). ANF, A=0.25°, k=0.1.
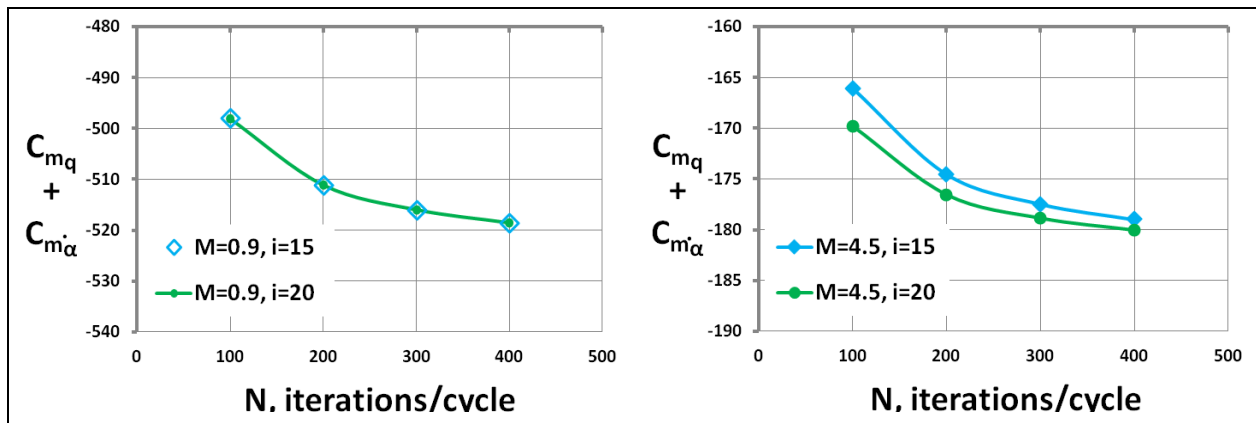
Figure 9. Effect of global iterations per cycle on PDM at Mach 0.9 (left) and Mach 4.5 (right). ANF, A=0.25°, k=0.1.

4.2.3 Amplitude and Frequency Dependence

Figure 10 shows the "pitching moment difference," $C_{m+} - C_{m-}$, as a function of pitch amplitude, A, and pitch frequency, k, for the ANF at Mach 0.9 and 4.5. The line plots are linear approximations using least squares linear regression fits. The regression correlation coefficient, R^2, values are indicated on the charts and are all very nearly equal to 1, indicating excellent linearity. According to equation 12, this implies that the PDF/M does not vary with pitch amplitude and frequency for the range of values tested herein. Similar results can be shown for the normal force difference, $C_{N+} - C_{N-}$. The nominal choices of $A = 0.25°$ and $k = 0.1$ used for all other simulations clearly lie within the linear range.
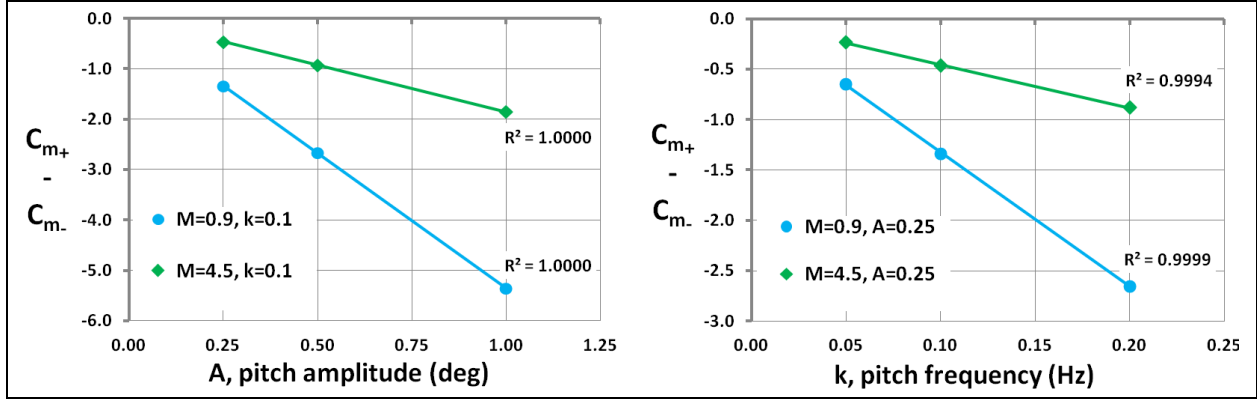
Figure 10. Effect of pitch amplitude, A, (left) and pitch frequency, k, (right). ANF, $N = 200$, $i = 20$.

Section 2.1 indicated that the normal force, C_N, and pitching moment, C_m, describe quasi-steady hystereses as function of angle of attack during the planar pitching oscillation. Figure 11 shows the effect of varying the amplitude on C_m at Mach 0.9 and 4.5 for the ANF. As a function of angle of attack, increasing the amplitude produces increasingly large concentric hysteresis curves all centered about $(\alpha_0, C_{m_0}) = (0,0)$. As a function of time, increasing the amplitude produces sinusoidal waves of the same frequency, but increasing wave amplitude. It is observed that initial transients are mitigated within a quarter of an oscillation, after which the solution becomes quasi-steady. Similar results can be shown for the C_N history as a function of amplitude.

Figure 12 shows the effect of varying the frequency on C_m for the ANF at Mach 0.9 and 4.5 for the ANF. As a function of angle of attack, increasing the frequency produces hysteresis curves with decreasing eccentricity all centered about $(\alpha_0, C_{m_0}) = (0,0)$. As a function of time, increasing the frequency increases the frequency and amplitude of the resulting sinusoidal waves. Again, it is observed that initial transients are mitigated within a quarter of an oscillation, after which the solution becomes quasi-steady. Similar results can be shown for the C_N history as a function of frequency.

20
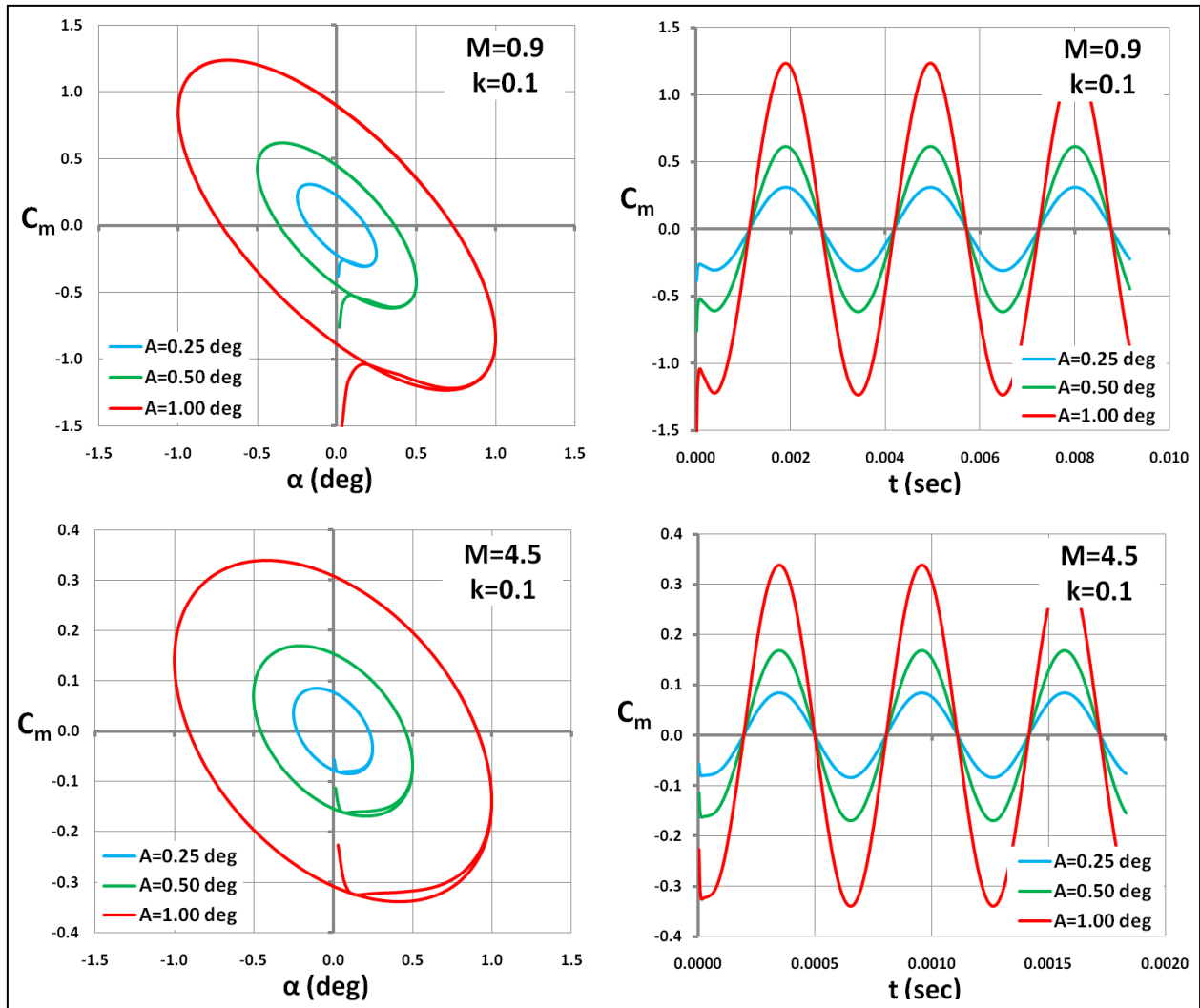
Figure 11. Effect of pitch amplitude, A, on pitching moment, C_m, as a function of angle of attack, α, (left) and time, t, (right). ANF, $k = 0.1$, $N = 200$, $i = 20$.
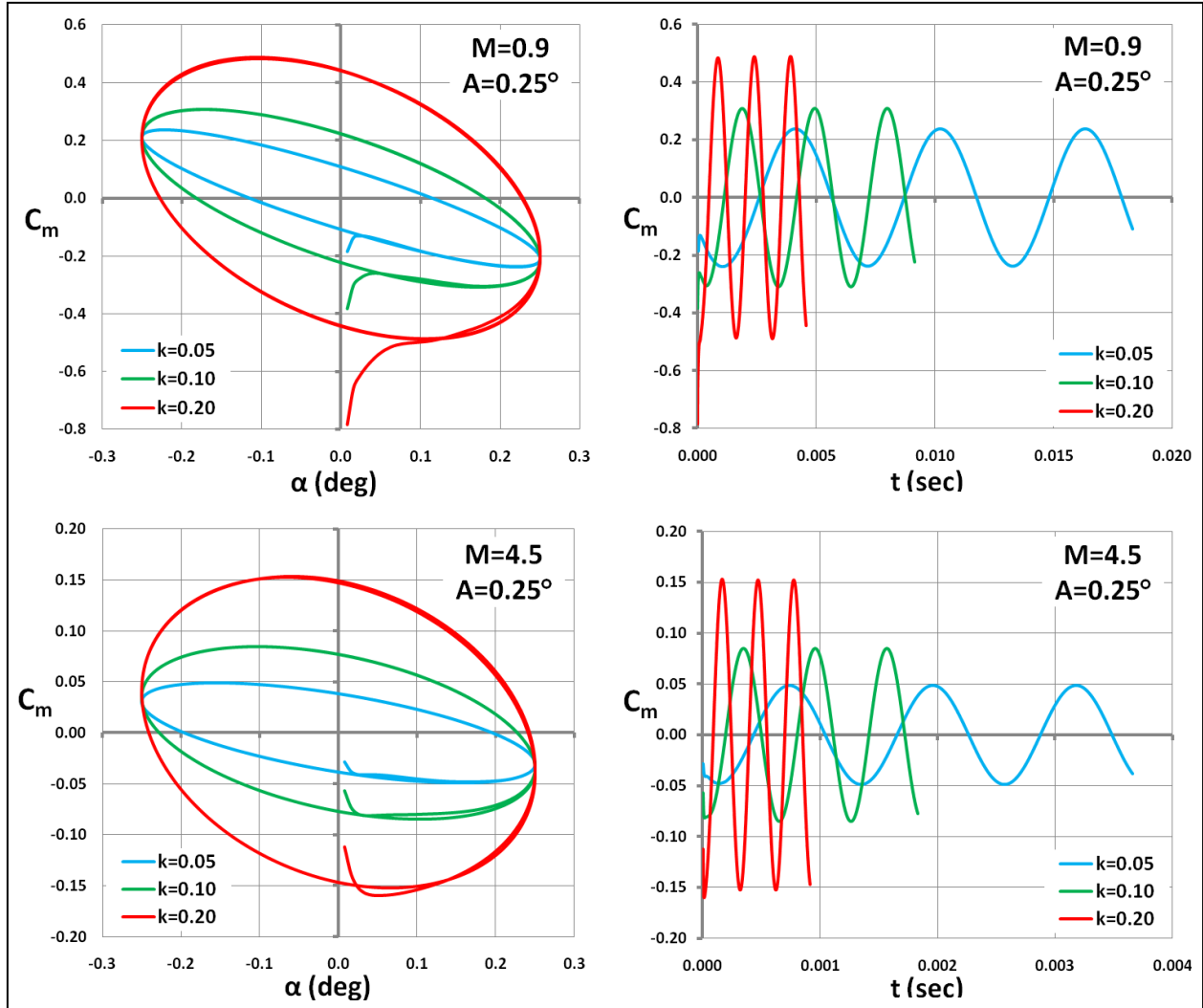
Figure 12. Effect of reduced pitch frequency, k, on pitching moment, C_m, as a function of angle of attack, α, (left) and time, t, (right). ANF, $A = 0.25$, $N = 200$, $i = 20$.

The results generally show that the nominal choices of $A = 0.25°$ and $k = 0.1$ provide adequate perturbation for computing the pitching damping derivatives while still satisfying the linear assumptions of the planar pitching method.

4.3   Steady Lunar Coning Parameter Study for ANF

4.3.1 General Trend, Grid Dependence, Effect of Fin Cant and Magnus Effect

Figure 13 shows the PDM sum, $C_{m_q} + C_{m_{\dot{\alpha}}}$, for Mach numbers in the range 0.5–4.5 computed via the lunar coning simulations for the ANF. Several numerical studies were conducted. The baseline case had coning angle $\alpha=0.5°$, coning rate $\Omega=0.0025$, fin cant $\delta=0°$, utilized the fine grid, and is represented by the red circles/red line in figure 13. Compared to DRDC free-flight data, baseline PDM values at subsonic velocities are about 102% larger in magnitude at Mach 0.766 (first free-flight multiple-fit data point). As previously discussed in section 4.2.1, the

source of the subsonic discrepancy is undetermined. Through the transonic region, 0.9<*M*<1.3, the CFD baseline predictions agree very well with the free-flight multiple-fit data points, except at Mach 1.105 where the free-flight multiple-fit data drops to -600. Above Mach 1.3, the CFD data generally show good to excellent agreement with the free-flight data.
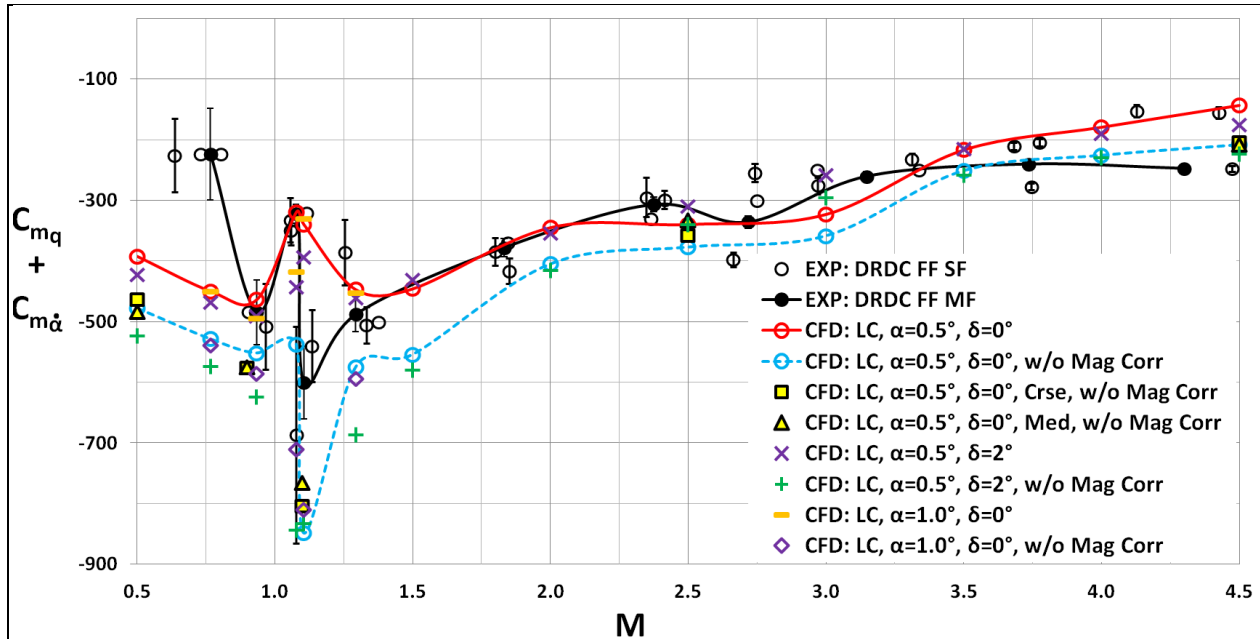
Figure 13. PDM as a function of Mach number – ANF lunar coning parameter study.

Figure 13 also shows the baseline case, but with a fin cant of $\delta = 2°$ (represented by the purple X*s*). The $\delta = 2°$ CFD data only slightly differ from the $\delta = 0°$ CFD data, except near Mach 1.1 where the difference reaches ~40% and between Mach 2.5 and 3.0 where the difference reaches ~25%.

As discussed in section 2.2, the Magnus force and moment components of the lunar coning motion in equations 18 and 20 were calculated via separate transient roll simulations. To investigate the significance of the Magnus terms using the lunar coning method on the pitch damping predictions, figure 13 shows the PDM for the baseline case with the Magnus moment assumed negligible, that is, with $C_{n_{p\alpha}}$=0 (blue circles/dashed blue line). In this case, it is observed that the magnitude of the PDM is overpredicted by ~20% in the subsonic region ($0.5 \le M \le 0.9$), ~150% at $M = 1.105$ and ~10%–30% in the supersonic region ($1.3 \le M \le 4.5$). The 2° canted fin results also show similar overpredictions of the PDM magnitude when the Magnus moment was assumed negligible (green +*s*). Except at Mach 1.105, the error differences between lunar coning with and without Magnus correction still lies within generally accepted error margins for free-flight experimental data. However, these error differences appear to be significantly larger for the finned projectiles studied herein than that suggested by some previous studies for axisymmetric projectiles (*11*).

23

Figure 13 and table 2 show the effect of grid resolution on the PDM predictions at specific Mach numbers of 0.5, 0.9, 1.1, 2.5, and 4.5. Note that the coarse grid (yellow squares) and medium grid (yellow triangles) results do not have the Magnus correction, and are thus compared to the fine grid baseline case without Magnus correction (blue circles/blue line). Except at Mach 2.5, the maximum difference between the fine and medium grid results is 3.3%. At Mach 2.5 the difference is 10.3%. Compromising between accuracy and computing efficiency, the fine grid was deemed acceptable for the lunar coning simulations.

Table 2. Lunar coning predictions: percent differences between fine, medium and coarse grid for ANF.

MACH NO.	LUNAR CONING			
	Difference Between **Fine & Medium** Grids		Difference Between **Fine & Coarse** Grids	
	PDF (%)	PDM (%)	PDF (%)	PDM (%)
0.5	0.23	1.15	3.12	3.03
0.9	1.46	2.33	0.96	2.47
1.1	2.63	3.28	1.56	1.63
2.5	10.30	11.71	6.27	4.98
4.5	0.64	0.18	3.34	2.24

4.3.2 Coning Rate and Coning Angle Dependence

The formulations presented in section 2.2 assumed that the side force and moment, C_Y and C_n, vary linearly with nondimensional coning rate, Ω. To determine a suitable range of Ω for which this linear assumption is satisfied Ω was varied as 0.001, 0.0025, 0.005, and 0.01. Figure 14 shows the variation of C_n with Ω for the uncanted ANF for Mach 0.5, 1.0, and 4.5 and nominal coning angle $\alpha = 0.5°$. The solid line plots are linear approximations using least-squares linear regression fits. For Mach 0.5 and 4.5, the regression correlation coefficient, R^2, values are nearly 1, indicating that C_n varies very linearly with Ω for Ω up to 0.01. For Mach 1.0, the solid green line was fitted only to the first three data points at which $\Omega = 0.001$, 0.0025, and 0.005. This solid green line was then extrapolated for visual comparison with a second-order polynomial regression approximation to all four Ω values (dashed green line). This was done to demonstrate the nonlinear variation of C_n with Ω for Ω beyond 0.005 at Mach 1.0. Similar trends can be shown for the variation of side force, C_Y, with Ω. Based on these results, a nominal coning rate of $\Omega=0.0025$ was chosen in order to satisfy the linearity assumptions for computing the PDF/M.

Note that in figure 14, the ordinate intercepts for the three Mach numbers are approximately zero – an intuitive outcome for a symmetric uncanted/unbeveled finner. This allows the computation of $\partial C_Y/\partial \Omega$ and $\partial C_n/\partial \Omega$ in equations 20 and 18 as simply C_Y/Ω and C_n/Ω, respectively. This also implies only a single simulation at a single coning rate within the linear range is needed to calculate the PDF/M given by equations 18 and 20 for a given freestream Mach number. For a canted finner, the ordinate intercept would be nonzero, and at least two simulations at two

different coning rates would be required to compute $\partial C_Y/\partial \Omega$ and $\partial C_n/\partial \Omega$. In this study, for the 2° canted ANF, the second coning rate was chosen as $\Omega = 0$, which equates to a static steady-state computation at a fixed angle of attack equal to the coning angle.
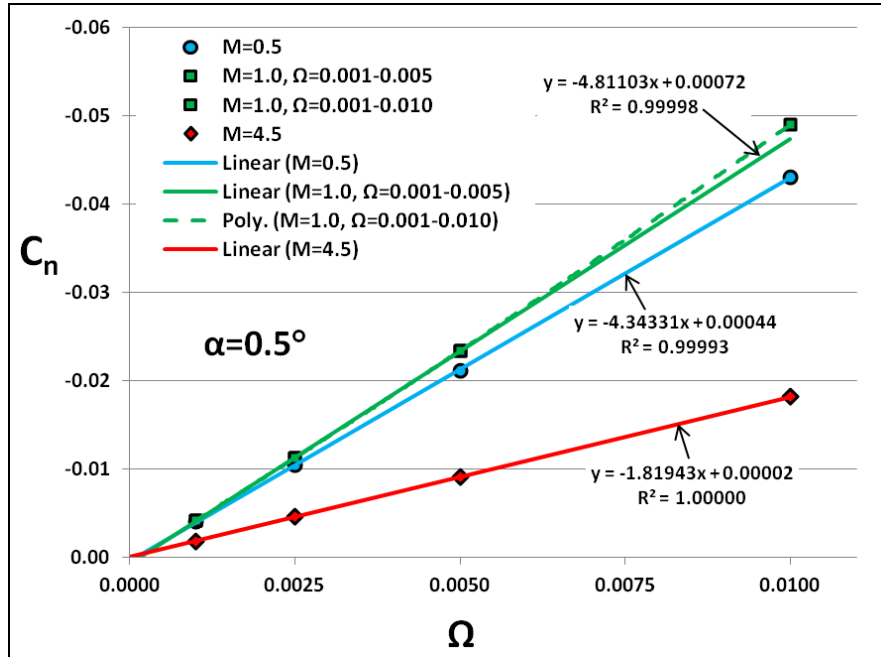
Figure 14. Variation of side moment, C_n, with coning rate, Ω, for the ANF, $\delta = 0°$.

The formulation of equations 18 and 20 implied that the side force and moment coning angle derivatives, $C_{Y_{\dot{\phi}}}$ and $C_{n_{\dot{\phi}}}$, vary linearly with σ, where σ is the sine of the coning angle, that is, $\sigma = \sin\alpha$. Figure 15 shows the variation of $C_{n_{\dot{\phi}}}$ with σ for Mach 0.5, 1.0, and 4.5, and nominal coning rate $\Omega = 0.0025$ for the uncanted ANF. The coning angle was varied as $\alpha = 0.25$, 0.50, 1.0, 2.0, and 3.0°. The solid line plots are linear approximations using least-squares regression fits. For Mach 0.5 and 4.5, the R^2 values are very nearly 1, indicating that $C_{n_{\dot{\phi}}}$ varies very linearly with σ for α up to 3° ($\sigma \approx 0.0523$). For Mach 1.0, the solid green line was fitted only to the first three data points for which $\alpha = 0.25$, 0.50, and 1.0° (i.e., up to $\sigma \approx 0.0175$). This solid green line was then extrapolated for visual comparison with a third-order polynomial regression approximation to all five σ values (dashed green line). This was done to demonstrate the nonlinear variation of $C_{n_{\dot{\phi}}}$ with σ for α beyond 1.0° at Mach 1.0. Similar trends can be shown for the variation of the side force derivative, $C_{Y_{\dot{\phi}}}$, with σ. Based on these results, a nominal coning angle of $\alpha = 0.5°$ ($\sigma \approx 0.00873$) was chosen in order to satisfy the linearity assumptions for computing the PDF/M.

25
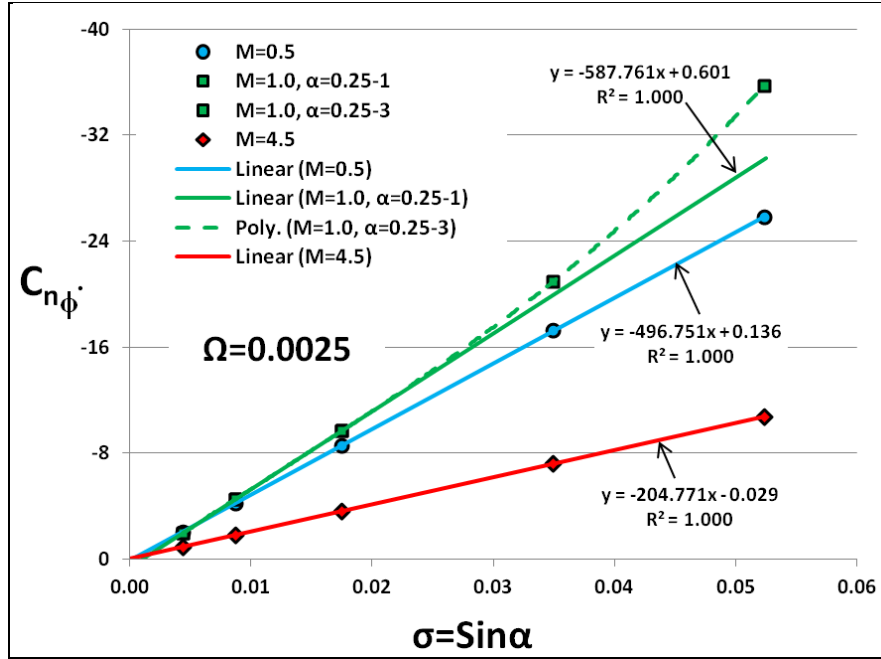
Figure 15. Variation of side moment slope, $C_{n_{\dot{\phi}}}$, with sine of the coning angle, σ, for the ANF.

Based on these results, the critical Mach regime for determining coning angles and coning rates in the linear range for the lunar coning method appears to be the transonic regime.

4.4 Final Pitch Damping Results for ANF and AFF: Comparing Planar Pitching and Lunar Coning Methods

The pitch damping force and moment results across the full Mach number regime for the ANF and AFF are compared below. These results were obtained using nominal modeling parameters. For the planar pitching simulations, nominal modeling parameters were as follows: inner timestep iterations $i = 20$, physical timestep iterations per pitch oscillation $N = 200$, pitch amplitude $A = 0.25°$ and reduced pitch frequency $k = 0.1$. For the lunar coning simulations, nominal modeling parameters were as follows: nondimensional coning rate $\Omega = 0.0025$ and coning angle $\alpha = 0.5°$.

Figure 16 compares the PDM between that obtained via the planar pitching and lunar coning CFD methods and DRDC free-flight data for the ANF. The 0° fin cant CFD data are considered first. Generally, both the planar pitching (red circles/red line) and lunar coning (blue diamonds/blue line) methods produce comparable results, except near Mach 1.1 and at Mach 2.5 and 3.0. Subsonically, for $M < 0.9$, there is a ~7% difference between the two CFD methods, however, as previously noted, both methods show a significant difference (>100%) from the DRDC free-flight data. Transonically, at M=0.934, both CFD methods compare very well with the multiple-fit free-flight data. At M=1.077, the lunar coning method matches the multiple-fit free-flight data, whereas the planar pitching method produces a ~50% larger magnitude. At M =

26

1.105, none of the three data sets match. As previously stated in section 3, the source/s of the discrepancies in the subsonic and transonic regions are undetermined, and additional free-flight data may be needed to validate the CFD methods. In the supersonic regime, above $M > 1.3$, both CFD methods generally compare very well with the free-flight data, however, there is a ~17% and ~25% difference between the two CFD methods at Mach 2.5 and 3.0, respectively.
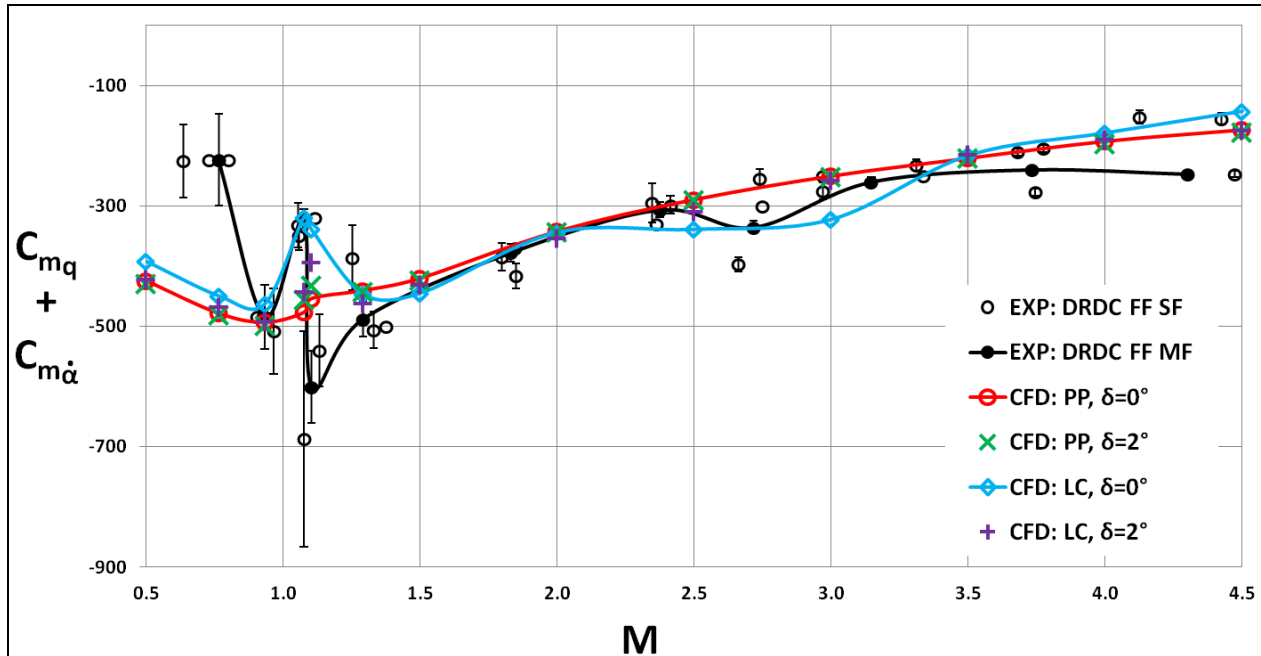
Figure 16. PDM sum variation with Mach number for ANF.

In the transonic regime, there is much scatter in the DRDC free-flight data with larger than normal standard deviation errors. The fluctuations/discrepancies in the free-flight data possibly indicate a dynamic instability. Based on a dynamic stability analysis, DRDC (*26*) suggested that a Magnus dynamic instability occurs in the transonic regime ($0.9 < M < 1.3$) and that the 4° fin cant models, and to a lesser extent the 2° fin cant models, were subject to this instability. Recall that the DRDC tests included fin cants of $\delta = 0$, 2, and 4°. In figure 16, the DRDC single-fit data include all three fin cants, whereas the multiple-fit data were derived from multiple data sets that included multiple fin cants; therefore any dynamic instabilities for the canted-fin models would be represented in figure 16.

The 2° canted fin CFD results computed via the planar pitching (green X*s*) and lunar coning (purple +*s*) methods match more closely with each other than the 0° canted fin CFD results, with the largest difference being ~10% at Mach 1.105. Except in the vicinity of Mach 1.1 and to a much lesser extent at Mach 2.5 and 3.0, the canted and uncanted PDM results are only slightly different.

Figure 17 compares the PDF between the planar pitching and lunar coning CFD methods for the ANF. No experimental data were available for comparison. For the uncanted fin, again, the two CFD methods (red and blue lines) are comparable, except in the vicinity of Mach 1.1 (~34% difference) and to a lesser extent at Mach 2.5–3.0 (~17%–27% difference). Like the PDM results, the 2° canted fin results for the two methods (green X*s* and purple +*s*) match more closely with each other, and, except in the vicinity of Mach 1.1, generally only slightly differ from the uncanted fin results.

Also shown in figure 17 are lunar coning PDF predictions without the Magnus correction for the uncanted and canted fins (pink dashed line and orange triangles, respectively). As observed in the PDM results of figure 13, figure 17 also demonstrates that ignoring the Magnus effect results in an overprediction of the PDF magnitude when using the lunar coning method; the difference is ~5% in the subsonic regime, ~117% at Mach 1.105, and ~10%–30% in the supersonic regime.
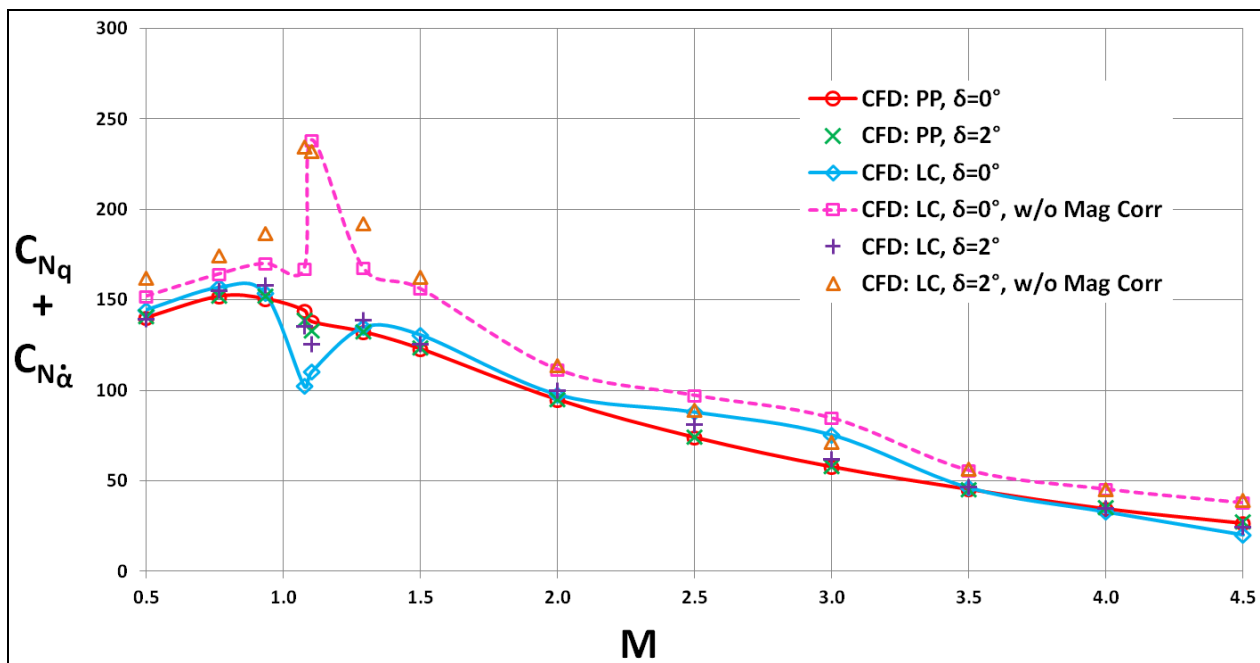
Figure 17. PDF sum variation with Mach number for ANF.

Figure 18 compares PDM results for the AFF obtained via the planar pitching and lunar coning CFD methods with DRDC and AFRL free-flight experimental data. In general, the planar pitching and lunar coning methods (red and blue lines) compare very well with each other particularly in the subsonic regime; between Mach 1.0 and 2.0 the disagreement is more notable where it reaches a maximum of ~30% at Mach 1.1; at Mach 2.5 the agreement is again very good.
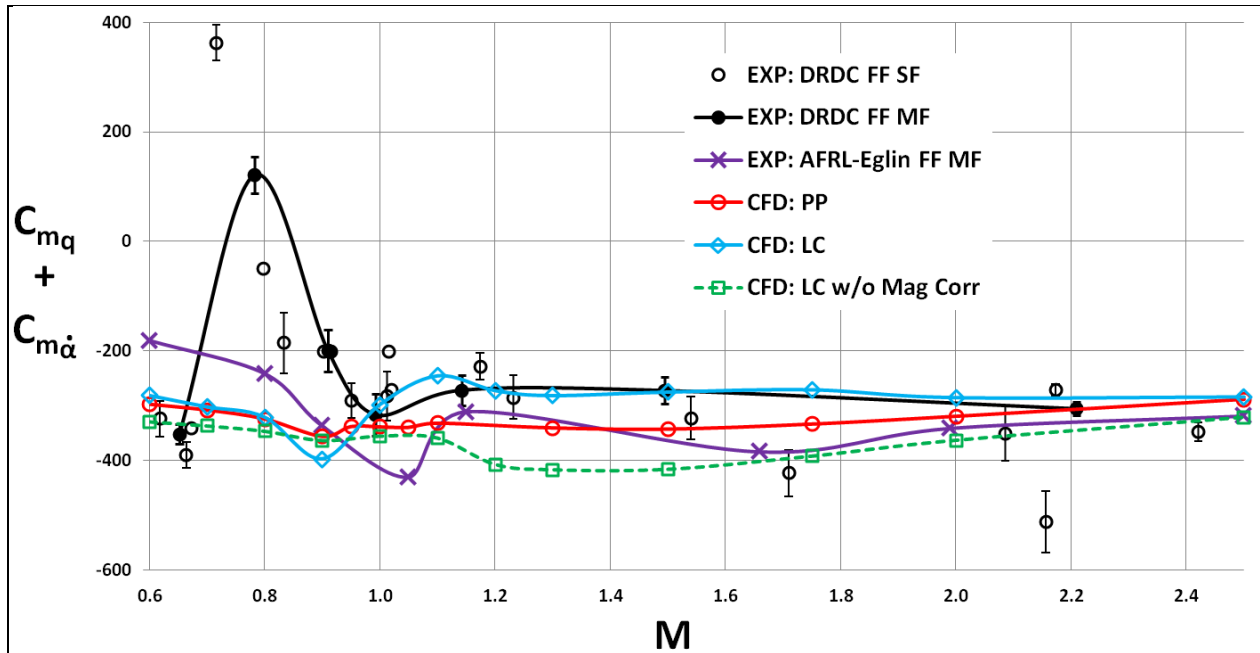
Figure 18. PDM sum variation with Mach number for AFF.

In the transonic and supersonic regimes above Mach 0.9, the AFRL data show a higher PDM magnitude than the DRDC multiple-fit data, reaching a difference of ~30% at Mach ~1.65. In these regimes, the lunar coning method generally matches the DRDC data better, whereas the planar pitching method (except at Mach 1.05) generally matches the AFRL data better.

In the subsonic regime below Mach 0.9, the PDM predicted by both CFD methods is larger in magnitude than the AFRL data, reaching a difference of ~60% at Mach 0.6. Between Mach 0.65 and 1.0, the DRDC data are grossly different from the AFRL and CFD data. In fact, the DRDC single-fit data point at Mach ~0.7 and multiple-fit data point at Mach ~0.8 show positive pitch damping, indicating dynamically unstable flight. According to DRDC (*28*), neither resonance nor Magnus effects were responsible for the pitch damping instability. Although the cause was therefore undetermined, it was conjectured to be damage to the test projectile, possibly on the fins. Note that for this AFF case, two different experimental data sets, viz, DRDC and AFRL, show very different pitch damping results in the subsonic region. The extent of the variability in the free-flight data sets in the subsonic and low transonic regions further supports the aforementioned conclusion that the accuracy of the CFD in this Mach number range is still inconclusive and additional experimental data are required.

Figure 18 also shows the lunar coning PDM results without the Magnus correction (dashed green line). As noted in results for the ANF, if the Magnus effect is ignored, the PDM magnitude is generally overpredicted; the difference is ~12% at Mach 0.7 and ~52% at Mach 1.5. There is one exception that occurs at Mach 0.9 where the PDM magnitude is underpredicted by ~10% without the Magnus correction.

Figure 19 compares the PDF between the planar pitching and lunar coning CFD methods for the AFF. No experimental data were available for comparison. Between Mach 0.6 and 1.0, the two methods (red and blue lines) show significant disagreement, reaching 24% difference at Mach 0.9. Above Mach 1.0, the disagreement is much less, reaching 12% at Mach 2.5. Considering all previous results, the disagreement in the subsonic region was higher than expected.
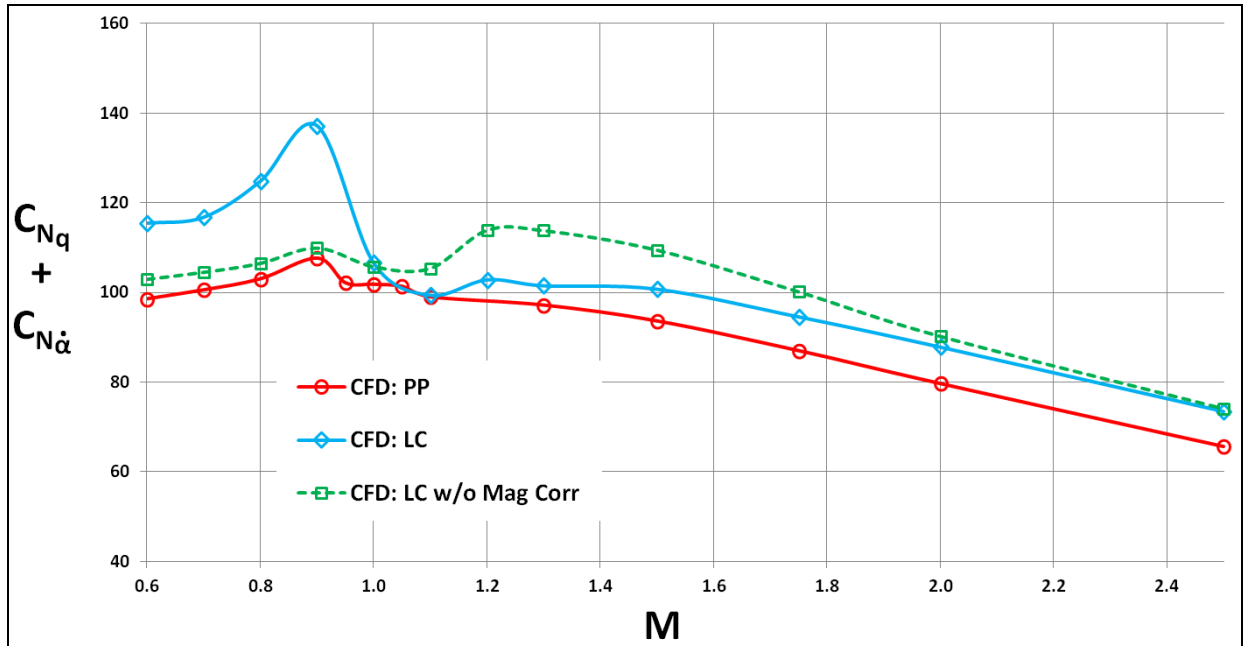
Figure 19. PDF sum variation with Mach number for AFF.

Also shown in figure 19 are lunar coning PDF results without the Magnus correction (dashed green line). Above Mach 1.0, the PDF magnitude without Magnus correction is overpredicted as expected, reaching ~12% difference at Mach 1.3. However, unlike previous trends, the PDF magnitude without Magnus correction is underpredicted below Mach 1.0, reaching ~25% difference at Mach 0.9. This behavior is yet to be further investigated.

5. Conclusion

RANS CFD and flight mechanics theory were used to compute the pitch damping dynamic stability derivatives via two distinct numerical techniques, viz, the time-accurate planar pitching method and the steady-state lunar coning method. The pitch damping force and moment were computed across the full Mach number regime for two basic finned projectiles, viz, the ANF and the AFF. Solution dependence on several aerodynamic and numerical modeling parameters was investigated. Numerical results, where available, were compared against free-

flight aeroballistic range data, as well as some wind-tunnel data, from Defense Research and Development Canada Valcartier Aeroballistic Range and Trisonic Wind-Tunnel Facilities in Quebec, Canada, and the U.S. AFRL ARF at Eglin Air Force Base, Florida.

For the planar pitching method, the pitch damping derivatives were shown to be related to the normal force and pitching moment for forced sinusoidal oscillation of the projectile. The pitch damping predictions were demonstrated to be fairly independent of the pitch amplitude and pitch frequency for linear variations of the normal force and pitching moment with amplitude and frequency. These linear variations were shown for amplitudes up to 1° and nondimensional frequencies up to 0.2 for the Army−Navy Finner. The limits of these linear variations will depend on projectile geometry and flight conditions, such as Mach number. The quasi-steady hysteresis variation of the normal force and pitching moment with angle of attack during the planar pitching motion was also demonstrated. The accuracy of the pitch damping predictions depended on the choices of physical timestep and inner iterations of the dual-timestep integration scheme used for solving the RANS equations. It was observed that the sensitivity of this dependence increases at higher freestream Mach numbers. Two hundred physical iterations per pitch cycle and twenty inner iterations were deemed sufficient for the computations herein, sacrificing only little accuracy for significant increases in computational efficiency. The Army−Navy Finner 2° fin cant appeared to have little or no effect on the pitch damping predictions computed via planar pitching. There was also little sensitivity of the planar pitching results to the three grid sizes tested herein for the Army−Navy Finner.

For the lunar coning method, the pitch damping derivatives were shown to be related to the total side force and moment, Magnus force and moment, and in the case of canted fins, to the side force and moment angle of attack derivatives. The pitch damping predictions were demonstrated to be independent of the coning angle and coning rate for linear variations of the side force and moment with coning rate and coning angle. These linear variations were investigated for coning angles up to 3° and nondimensional coning rates up to 0.01 for the Army−Navy Finner. The linear assumptions degenerated at smaller coning angles and coning rates for the transonic Mach regime than for the subsonic and supersonic regimes. The Magnus effect as a result of the lunar coning motion on the pitch damping predictions was shown to be significant for both finned projectiles, particularly in the transonic Mach regime. Assuming the Magnus effect to be negligible usually resulted in an overprediction of the pitch damping force and moment magnitudes, except for the pitch damping force for the Air Force Finner below Mach 1.0. The Magnus terms were determined via separate time-dependent axial roll simulations. Since no parametric studies were conducted for the latter, the accuracy of the Magnus computations is yet to be verified – an exercise left for a future study. The Army−Navy Finner 2° fin cant appeared to have little effect on the pitch damping predictions computed via lunar coning, except in the transonic regime where the difference was more notable. Except at one supersonic Mach number, the lunar coning results were shown to be fairly grid-independent of the three grid levels tested.

Generally, the two numerical techniques—planar pitching and lunar coning—yielded fairly comparable results across most of the Mach number range. The largest differences between the two techniques occurred in the transonic regime, particularly for the Army−Navy Finner. Compared to free-flight test data, both techniques generally show good agreement in the high transonic and supersonic regimes, but poor agreement in the subsonic and low transonic regimes. In the subsonic and low transonic regimes, the accuracy of the free-flight test data was uncertain due to instances of large scatter, large standard deviation errors and different data sources showing significantly different results. The variability of the free-flight data therefore necessitates additional experimental data to validate the numerical methods.

Regarding computational effort, the planar pitching method requires only a single time-accurate oscillatory computation, whereas the lunar coning method requires a steady-state coning computation plus a time-accurate rolling computation to account for the Magnus effect. Because the Magnus effect during coning can be significant even for a finned projectile, the planar pitching method offers a more efficient method of computing the pitch damping derivatives than the lunar coning method. Also, the Magnus effect can be difficult to compute accurately for some projectiles at subsonic and transonic speeds—a source of error that the planar pitching method does not inherit. However, if full aerodynamic characterization of a projectile is needed, the time-accurate rolling computations would have to be conducted regardless to compute the roll damping and Magnus derivatives, in which case either planar pitching or lunar coning to compute the pitch damping derivatives may equally suffice.

6. References

1. Bhagwandin, V. A; Sahu, J. Numerical Prediction of Pitch Damping Derivatives for a Finned Projectile at Angles of Attack. *AIAA Aerospace Sciences Meeting*, AIAA 2012-691, Nashville, TN, January 2012.

2. Bhagwandin, V. A.; Sahu, J. Numerical Prediction of Pitch Damping Stability Derivatives for Finned Projectiles. *AIAA Applied Aerodynamics Conference*, AIAA 2011-3028, Honolulu, HI, June 2011.

3. McGowan, G. Z.; Kurzen, M. J.; Nance, R. P.; Carpenter, J. G.; Moore, F. G. Computational Investigation of Pitch Damping on Missile Geometries at High Angles of Attack. *AIAA Applied Aerodynamics Conference*, AIAA 2012-2903, New Orleans, LA, June 2012.

4. Murman, S. M. Reduced-Frequency Approach for Calculating Dynamic Derivatives. *AIAA Journal* **2007**, *45* (6), 1161–1168.

5. Oktay, E.; Akay, H. CFD Predictions Of Dynamic Derivatives for Missiles. *AIAA Aerospace Sciences Meeting*, AIAA 2002-0276, Reno, NV, January 2002.

6. Park, S. H.; Kim, Y.; Kwon, J. H. Prediction of Damping Coefficients Using the Unsteady Euler Equations. *AIAA Journal of Spacecraft and Rockets* May-June **2003**, *40* (3), 356–362.

7. Park, S. H.; Kwon, J. H.; Kim, Y. Prediction of Dynamic Damping Coefficients Using Unsteady Dual-Time Stepping Method. *AIAA Aerospace Sciences Meeting*, AIAA 2002-0715, Reno, NV, January 2002.

8. Sahu, J. Numerical Computations of Dynamic Derivatives of a Finned Projectile Using a Time-Accurate CFD Method. *AIAA Atmospheric Flight Mechanics Conference*, AIAA 2007-6581, August 2007.

9. Stalnaker, J. F.; Robinson, M. A. Computation of Stability Derivatives of Spinning Missiles Using Unstructured Cartesian Meshes. *AIAA Applied Aerodynamics Conference*, AIAA 2002-2802, St. Louis, MO, June 2002.

10. Weinacht, P. Characterization of Small-Caliber Ammunition Performance Using a Virtual Wind Tunnel Approach. *AIAA Atmospheric Flight Mechanics Conference*, AIAA 2007-6579, Hilton Head, SC, August 2007.

11. DeSpirito, J.; Silton, S, I.; Weinacht, P. Navier-Stokes Predictions of Dynamic Stability Derivatives: Evaluation of Steady-State Methods. *AIAA Journal of Spacecraft and Rockets* November-December **2009**, *46* (6), 1142–1154.

12. Agarwal, R.; Rakich, J. V. Computation of Supersonic Laminar Viscous Flow Past a Pointed Cone at Angle of Attack in Spinning and Coning Motion. *AIAA Fluid and Plasma Dynamics Conference*, AIAA 78-1211, Seattle, WA, July 1978.

13. Lin, T. C. Numerical Study of Re-entry Vehicle Aerodynamics in Steady Coning Motion. *AIAA Journal of Spacecraft and Rockets* May **1981**, *18* (3), 228–234.

14. Levy, L. L.; Tobak, M. Nonlinear Aerodynamics of Bodies of Revolution in Free Flight. *AIAA Journal* **1970**, *8* (12), 2168–2171.

15. Schiff, L. B. Nonlinear Aerodynamics of Bodies in Coning Motion. *AIAA Journal* November **1972**, *10* (11), 1517–1522.

16. Schiff, L. B.; Tobak, M. Results from a New Wind-Tunnel Apparatus for Studying Coning Motions of Bodies of Revolution. *AIAA Journal* November **1970**, *8* (11), 1953–1957.

17. Tobak, M.; Schiff, L. B. Generalized Formulation of Nonlinear Pitch-Yaw-Roll Coupling: Part I—Nonaxisymmetric Bodies. *AIAA Journal* March **1975**, *13*, (3), 323–326.

18. Tobak, M.; Schiff, L. B.; Generalized Formulation of Nonlinear Pitch-Yaw-Roll Coupling: Part II—Nonlinear Coning Rate. *AIAA Journal* March **1975**, *13* (3), 327–332.

19. Tobak, M.; Schiff, L. B.; Peterson, V. L. Aerodynamics of Bodies of Revolution in Coning Motion. *AIAA Journal* January **1969**, *7* (1), 95–99.

20. Weinacht, P.; Sturek, W. B. Navier-Stokes Predictions of Pitch Damping for Finned Projectiles using Steady Coning Motion. *AIAA Applied Aerodynamics Conference*, AIAA 90-3088, Portland, OR, August 1990.

21. Weinacht, P.; Sturek, W. B.; Schiff, L. B. Navier-Stokes Predictions of Pitch Damping for Axisymmetric Projectiles. *AIAA Journal of Spacecraft and Rockets* November–December **1997** *34* (6), 753–761.

22. Carlucci, D. E.; Jacobson, S. S. *Ballistics: Theory and Design of Guns and Ammunition*; Taylor & Francis Group; CRC Press: Boca Raton, FL, 2008.

23. McCoy, R. L. *Modern Exterior Ballistics*, Schiffer Publishing Ltd.: Atglen, PA, 1999.

24. Murphy, C. H. *Free-Flight Motion of Symmetric Missiles*; BRL-1216; U.S. Army Research Laboratory: Aberdeen Proving Ground, MD, July 1963.

25. Metacomp Technologies, Inc., *CFD++ User Manual*, Agoura Hills, CA, 2007.

26. Dupuis, A. D.; Hathaway, W. *Aeroballistic Range Tests of the Basic Finner Reference Projectile at Supersonic Velocities*; DREV-TM-9703; Defense Research Establishment: Valcartier, Canada, August 1997.

27. Dupuis, A. *Aeroballistic Range and Wind Tunnel Tests of the Basic Finner Reference Projectile From Subsonic to High Supersonic Velocities*; TM 2002-136; Defense Research & Development: Canada, Valcartier, October 2002.

28. Dupuis, A. D.; Hathaway, W. Aeroballistic Range Tests of the Air Force Finner Reference Projectile; TM 2002-008; Defense Research & Development: Canada, Valcartier, May 2002.

29. West, K. O. *Comparison of Free-flight Spark Range and Wind Tunnel Test Data for a Generic Missile Configuration at Mach Numbers From 0.6 to 2.5*; AFATL-TR-81-87; Air Force Armament Laboratory: Eglin Air Force Base, FL, October 1981.

30. Bhagwandin, V. A. Numerical Prediction of Roll Damping and Magnus Dynamic Derivatives for Finned Projectiles at Angle of Attack. *AIAA Applied Aerodynamics Conference*, AIAA 2012-2905, New Orleans, LA, June 2012.

31. Pointwise, Inc. *Pointwise User Manual*, Fort Worth, TX, 2010.

32. Chien, K.-Y. Predictions of Channel and Boundary Layer Flows with a Low-Reynolds-Number Turbulence Model. *AIAA Journal* **1982**, *20* (1), 33–38.

INTENTIONALLY LEFT BLANK.

Appendix. CFD Pitch Damping Data

Table A-1. CFD results – pitch damping vs. Mach number, Army-Navy basic finner (fine grid).

| M | Planar Pitching, *A*=0.25, *k*=0.1 | | | | [a]Lunar Coning, *σ*=0.5°, *Ω*=0.0025 | | | |
| | *δ*=0° | | *δ*=4° | | *δ*=0° | | *δ*=4° | |
	PDM	PDF	PDM	PDF	PDM	PDF	PDM	PDF
0.50	–427.81	141.90	–432.03	142.63	–392.14	144.71	–422.55	139.55
0.77	–480.28	152.95	–482.34	153.36	–449.81	157.15	–467.60	155.59
0.93	–494.30	151.21	–498.69	152.54	–463.48	153.81	–490.93	158.17
1.08	–478.35	144.87	–457.47	139.75	–319.49	102.79	–443.04	135.57
1.11	–454.43	138.48	–431.57	133.53	–339.80	110.48	–393.84	125.95
1.29	–440.19	132.62	–441.68	133.01	–447.12	135.09	–461.24	139.33
1.50	–419.52	123.33	–422.17	124.15	–445.80	130.95	–430.73	125.61
2.00	–341.93	95.02	–343.28	95.46	–344.75	97.97	–353.99	100.01
2.50	–288.89	73.99	–289.96	74.39	–339.60	88.23	–309.31	81.38
3.00	–249.34	57.65	–250.70	58.16	–323.06	75.61	–258.11	62.44
3.50	–219.92	45.13	–220.43	45.42	–216.74	46.43	–214.55	46.89
4.00	–192.52	34.48	–196.60	35.41	–179.19	33.06	–189.72	34.90
4.50	–173.53	26.52	–177.05	27.47	–143.24	20.38	–175.08	24.96

Table A-2. CFD results – pitch damping vs. Mach number, Air Force modified finner.

| M | Planar Pitching, *A*=0.25, *k*=0.1 | | [a]Lunar Coning, *σ*=0.5°, *Ω*=0.0025 | |
| | *δ*=0° | | *δ*=0° | |
	PDM	PDF	PDM	PDF
0.60	–297.42	98.54	–280.74	115.45
0.70	–307.85	100.53	–301.66	116.78
0.80	–323.72	102.98	–320.50	124.79
0.90	–355.21	107.59	–397.20	137.17
0.95	–337.55	102.11	–297.70	106.60
1.00	–338.09	101.77	–244.68	99.40
1.05	–339.05	101.31	–271.70	102.84
1.10	–331.43	98.98	–281.05	101.53
1.30	–339.94	97.14	–274.58	100.75
1.50	–342.18	93.62	–270.38	94.59
1.75	–333.02	87.01	–284.81	87.86
2.00	–319.02	79.69	–283.53	73.53
2.50	–288.64	65.69	–280.74	115.45

[a]Pitch damping data for lunar coning results includes Magnus correction.

List of Symbols, Abbreviations, and Acronyms

C_j	arbitrary force or moment coefficient, $j=X, Y, N, m, n$
C_{j_0}	arbitrary force or moment coefficient at zero angle of attack or zero spin rate
C_{j_k}	arbitrary force or moment coefficient derivative with respect to k, $k=\alpha, \dot{\alpha}, q, \dot{\phi}$
$C_{j_{k_0}}$	arbitrary force or moment coefficient derivative with respect to k at zero angle of attack
$C_{N_q} + C_{N_{\dot{\alpha}}}$	pitch damping force coefficient sum, or PDF
$C_{m_q} + C_{m_{\dot{\alpha}}}$	pitch damping moment coefficient sum, or PDM
C_{N+}	normal force coefficient at mean angle of attack during planar pitching-up motion
C_{N-}	normal force coefficient at mean angle of attack during planar pitching-down motion
C_{m+}	pitching moment coefficient at mean angle of attack during planar pitching-up motion
C_{m-}	pitching moment coefficient at mean angle of attack during planar pitching-down motion
$C_{Y_{p\alpha}}$	Magnus force coefficient due to coning motion
$C_{n_{p\alpha}}$	Magnus moment coefficient due to coning motion
α	angle of attack/coning angle, rad or deg
α_0	mean angle of attack during planar pitching motion, rad or deg
$\dot{\alpha}$	time rate of change of angle of attack or plunge rate, rad/s
q	time rate of change of pitch or pitch rate, rad/s
A	pitching amplitude, rad or deg
ω	planar pitching angular frequency, rad/s
f	pitching frequency, Hz
k	nondimensional/reduced pitching frequency
t	time, s

T	period of pitch/roll cycle, s
Δt	transient global/physical timestep, s
N	global iterations per pitch cycle
i	number of inner iterations per global iteration
n	integer count for each half of a pitch cycle
$\dot{\phi}$	angular coning rate, rad/s
Ω	nondimensional coning rate
p	angular roll rate or spin rate, rad/s
ρ	freestream density, kg/m^3
M	freestream Mach number
V	freestream velocity, m/s
P_S	static pressure, Pa
T_S	static temperature, K
k	turbulent kinetic energy, m^2/s^2
ε	turbulent dissipation rate, m^2/s^3
D	projectile base diameter = 1 caliber, m
S	reference surface area = $\pi D^2/4$, m^2
δ	fin cant angle
$y+$	nondimensional wall distance
σ	sine of angle of attack = $\sin \alpha$
γ	cosine of angle of attack = $\cos \alpha$
R	least squares regression correlation coefficient

Subscripts

X	axial force
Y	side force
N	normal force

m	pitching moment
n	side moment

Abbreviations

6-DOF	six-degree-of-freedom
AFF	Air Force Modified Basic Finner
AFRL	U.S. Air Force Research Laboratory
ANF	Army−-Navy Basic Finner
ARF	Aeroballistic Research Facility
ARL	U.S. Army Research Laboratory
CFD	computational fluid dynamics
CFL	Courant−Friedrichs−Lewy
DRDC	Defense Research and Development Canada
FF	free-flight
HLLC	Harten−Lax−van Leer−Contact
HPCMP	High Performance Computing Modernization Program
LC	lunar coning
MF	multiple-fit (free-flight data)
PDF	pitch damping force
PDF/M	pitch damping force and moment
PDM	pitch damping moment
PP	planar pitching
RANS	Reynolds-Averaged Navier−-Stokes
SF	single-fit (free-flight data)
SS	steady-state
WT	wind tunnel

NO. OF COPIES	ORGANIZATION
1 (PDF)	DEFENSE TECHNICAL INFORMATION CTR DTIC OCA
1 (PDF)	DIRECTOR US ARMY RESEARCH LAB IMAL HRA
1 (PDF)	DIRECTOR US ARMY RESEARCH LAB RDRL CIO LL
1 (PDF)	GOVT PRINTG OFC A MALHOTRA
2 (PDF)	NAWCWD P CROSS R SCHULTZ
2 (PDF)	RDECOM AMRDEC L AUMAN M MCDANIEL
8 (PDF)	RDECOM ARDEC D CARLUCCI S CHUNG D CLER M DUCA J GRAU W KOENIG W TOLEDO C WILSON
1 (PDF)	AEROPREDICTION INC F MOORE
1 (PDF)	ARROW TECH W HATHAWAY
2 (PDF)	DRDC D CORRIVEAU N HAMEL
2 (PDF)	DSTL R CHAPLIN B SHOESMITH
1 (PDF)	DSTO M GIACOBELLO
1 (PDF)	MARTEC LIMITED D ALLEXANDER

NO. OF COPIES	ORGANIZATION
1 (PDF)	NASA S VIKEN
3 (PDF)	NAVAIR J LEE T SHAFER D FINDLAY
1 (PDF)	ISL C BERNER

ABERDEEN PROVING GROUND

28 (PDF)	RDRL WM P BAKER R EHLERS P PLOSTINS RDRL WML P PEREGINO M ZOLTOSKI RDRL WML A W OBERLE RDRL WML B N TRIVEDI RDRL WML C S AUBERT RDRL WML D R BEYER RDRL WML E V BHAGWANDIN I CELMINS J DESPIRITO L FAIRFAX F FRESCONI J GARNER B GUIDOS K HEAVEY R KEPPINGER G OBERLIN T PUCKETT J SAHU S SILTON P WEINACHT RDRL WML F B DAVIS RDRL WML G J SOUTH RDRL WML H J NEWILL RDRL WMM J ZABINSKI RDRL WMP D LYON